Neurobiology of Disease 182 (2023) 106151

Contents lists available at ScienceDirect

Neurobiology of Disease

journal homepage: www.elsevier.com/locate/ynbdi

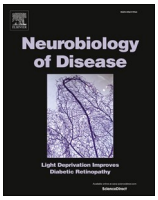

Alterations to parvalbumin-expressing interneuron function and associated network oscillations in the hippocampal – medial prefrontal cortex circuit during natural sleep in App$^{NL\text{-}G\text{-}F/NL\text{-}G\text{-}F}$ mice

Erica S. Brady [a,b], Jessica Griffiths [a,c], Lilya Andrianova [a,d], Monika H. Bielska [d], Takashi Saito [e], Takaomi C. Saido [f], Andrew D. Randall [a,g], Francesco Tamagnini [a,c], Jonathan Witton [a,**], Michael T. Craig [a,d,*]

[a] Institute of Biomedical and Clinical Science, University of Exeter Medical School, Prince of Wales Road, Exeter EX4 4PS, England, UK
[b] Gladstone Institute for Neurological Disease, 1650 Owens Street, San Francisco, CA 91458, United States of America
[c] School of Pharmacy, University of Reading, Whiteknights, Reading RG6 6LA, UK
[d] School of Psychology and Neuroscience, College of Medical, Veterinary and Life Sciences, University of Glasgow, Glasgow G12 8QQ, Scotland, UK
[e] Department of Neurocognitive Science, Institute of Brain Science, Nagoya City University Graduate School of Medical Sciences, Japan
[f] Laboratory for Proteolytic Neuroscience, RIKEN Center for Brain Science, Saitama 351-0198, Japan
[g] School of Physiology and Pharmacology, University of Bristol, Bristol BS8 1TD, UK

ARTICLE INFO

Keywords:
Alzheimer's disease
Neuronal oscillation
Parvalbumin interneuron
Amyloid

ABSTRACT

In the early stages of Alzheimer's disease (AD), the accumulation of the peptide amyloid-β (Aβ) damages synapses and disrupts neuronal activity, leading to the disruption of neuronal oscillations associated with cognition. This is thought to be largely due to impairments in CNS synaptic inhibition, particularly via parvalbumin (PV)-expressing interneurons that are essential for generating several key oscillations. Research in this field has largely been conducted in mouse models that over-express humanised, mutated forms of AD-associated genes that produce exaggerated pathology. This has prompted the development and use of knock-in mouse lines that express these genes at an endogenous level, such as the App$^{NL\text{-}G\text{-}F/NL\text{-}G\text{-}F}$ mouse model used in the present study. These mice appear to model the early stages of Aβ-induced network impairments, yet an in-depth characterisation of these impairments in currently lacking. Therefore, using 16 month-old App$^{NL\text{-}G\text{-}F/NL\text{-}G\text{-}F}$ mice, we analysed neuronal oscillations found in the hippocampus and medial prefrontal cortex (mPFC) during awake behaviour, rapid eye movement (REM) and non-REM (NREM) sleep to assess the extent of network dysfunction. No alterations to gamma oscillations were found to occur in the hippocampus or mPFC during either awake behaviour, REM or NREM sleep. However, during NREM sleep an increase in the power of mPFC spindles and decrease in the power of hippocampal sharp-wave ripples was identified. The latter was accompanied by an increase in the synchronisation of PV-expressing interneuron activity, as measured using two-photon Ca^{2+} imaging, as well as a decrease in PV-expressing interneuron density. Furthermore, although changes were detected in local network function of mPFC and hippocampus, long-range communication between these regions appeared intact. Altogether, our results suggest that these NREM sleep-specific impairments represent the early stages of circuit breakdown in response to amyloidopathy.

Abbreviations: AD, Alzheimer's disease; Aβ, amyloid-β; PV, parvalbumin; mPFC, medial prefrontal cortex; REM, rapid eye movement; NREM, non-rapid eye movement; SWO, slow wave oscillation; SWR, sharp-wave ripples; WT, wildtype; LEDs, light-emitting diodes; PB, phosphate buffer; PFA, paraformaldehyde; PBS, phosphate buffered saline; ACC, anterior cingulate cortex; PL, prelimbic cortex; LFP, local field potential; *Str.P*, *Stratum pyramidale*; PAC, phase-amplitude coupling; ROI, regions of interest; ΔF/F, fluorescence time series; PBS-T, PBS with 0.3% Triton X-100; IQR, inter-quartile range; O-LM, *oriens-lacunosum moleculare*; UDS, Up and Down states; TRN, thalamic reticular nucleus.

* Corresponding author at: School of Psychology and Neuroscience, College of Medical, Veterinary and Life Sciences, University of Glasgow, Glasgow G12 8QQ, Scotland, UK.
** Corresponding author.
E-mail addresses: j.witton@exeter.ac.uk (J. Witton), mick.craig@glasgow.ac.uk (M.T. Craig).

https://doi.org/10.1016/j.nbd.2023.106151
Received 11 January 2023; Received in revised form 7 May 2023; Accepted 9 May 2023
Available online 10 May 2023

1. Introduction

Alzheimer's disease (AD) is a progressive neurodegenerative disorder and the most prevalent form of dementia worldwide (Nichols et al., 2019). In the preclinical stages of the disease, preceding overt signs of cognitive decline, the build-up and aggregation of the peptide amyloid-β (Aβ) causes detriment to the synapse and neuronal activity, before accumulating further to form the extracellular plaque pathology that characterises AD. In turn, these detriments disrupt the synchronous communication between groups of neurons that generate the neuronal oscillations associated with cognitive function (Busche et al., 2012; Busche et al., 2008; Hsieh et al., 2006; Shankar et al., 2007; Palop et al., 2007; Chung et al., 2020). These impairments to the electrical activity of the brain can be measured in humans as hyperactivity of the hippocampus and areas of the default mode network (Sperling et al., 2009; Bakker et al., 2012) and lead to the generation of epileptiform activity (Born, 2015) and a general "slowing" of the EEG (Dauwels et al., 2011). Evidence suggests that altered inhibitory neurotransmission underlies this breakdown in circuit function (Palop and Mucke, 2016). In particular, parvalbumin (PV)-expressing interneurons have been shown to exhibit both hypo- and hyperactivity in mouse models of amyloidopathy (Verret et al., 2012; Martinez-Losa et al., 2018; Hijazi et al., 2019), with the former being linked to a reduction in the amplitude of gamma oscillations and the emergence of epileptic spikes.

Sleep disturbances, particularly disruptions to the quality and duration of non-rapid eye movement (NREM) sleep, are also a common feature during the early stages of AD, and are strongly linked to cognitive decline (Bubu et al., 2017; Sindi et al., 2018). Importantly, the long-term consolidation of memory is thought to occur during NREM sleep, with significant research emphasis being placed on the activity of the hippocampal – medial prefrontal cortex (mPFC) circuit, given its prominent roles in episodic and spatial memory, as well as higher-order executive functions (Sigurdsson and Duvarci, 2015; Rasch and Born, 2013). The generation and temporal coupling of three cardinal neuronal oscillations – the cortical slow wave oscillation (SWO), spindles, and hippocampal sharp-wave ripples (SWR) – facilitates the reorganisation of newly encoded hippocampal memories into distributed cortical networks for long-term storage, in a process called systems consolidation (Crunelli and Hughes, 2010; Maingret et al., 2016). Perturbation of the SWO and spindles is observed in humans with AD (Mander et al., 2015a; Kam et al., 2019), with similar disruptions to the SWO occurring in mouse models of amyloidopathy (Castano-Prat et al., 2019; Busche et al., 2015; Kastanenka et al., 2017), alongside impairments to SWRs (Caccavano et al., 2020).

Understanding neuronal network dysfunction in the preclinical stages of AD is imperative for the identification of early-detection biomarkers and for the development of treatments to be delivered prior to the occurrence of irreversible neurodegeneration and cognitive decline. However, the majority of research to date has been conducted in transgenic mouse models that develop exaggerated pathology due to the over-expression of humanised, mutated AD-linked genes that are co-expressed alongside murine homologs (Sasaguri et al., 2017). Indeed, the widespread use of such over-expression models may provide one explanation why experimental pharmaceutical interventions that show efficacy in mice have commonly failed in phase III clinical trials (Sasaguri et al., 2017). This has prompted the innovation of knock-in lines that have had the endogenous mouse gene replaced with the human homolog, thus achieving physiological levels of expression (Sasaguri et al., 2017; Nilsson et al., 2014). Conducting experiments in knock-in mouse models that are not confounded by non-physiological over-expression of mutated genes should provide researchers with a greater understanding of how early Aβ pathology alters brain physiology. With this in mind, we analysed the neuronal oscillatory activity of the hippocampal-mPFC circuit in sixteen-month-old $App^{NL\text{-}G\text{-}F/NL\text{-}G\text{-}F}$ mice across three different brain states: awake behaviour, rapid-eye movement (REM) and NREM sleep. Our goal was to assess Aβ-induced network dysfunction before cognitive decline, and to determine whether this dysfunction displayed brain region- and state-specific effects.

2. Methods

2.1. Animals

For use in this study, heterozygous $App^{NL\text{-}G\text{-}F/WT}$ mice (originally obtained from the MRC Harwell Institute, bred internally, and maintained on a C57BL/6J background) were cross-bred to obtain male and female, sixteen-month-old homozygous $App^{NL\text{-}G\text{-}F/NL\text{-}G\text{-}F}$ mice (APP) and wildtype (WT) littermate controls (Nilsson et al., 2014; Saito et al., 2014). All animals were housed on a 12-h light-dark cycle at a temperature of 22 ± 2 °C and humidity of 45 ± 15% and had *ad libitum* access to food and water. For electrophysiological studies, $N = 6$ mice per genotype were implanted with electrodes but due to post-operative complications, $N = 5$ mice per genotype were used for experiments (WT: 2 male, 3 female; APP: 3 male, 2 female). $N = 7$ WT (5 male, 2 female) and N = 7 APP (3 male, 4 female) were used for immunohistochemical analysis. For two-photon imaging, APP mice were crossbred with mice expressing Cre recombinase in parvalbumin-expressing interneurons (PV-cre mice; The Jackson Laboratory, #008069) or somatostatin-expressing interneurons (SST-cre mice; The Jackson Laboratory, #013044) to generate App^{HOM}::PV-cre (PVAPP) and App^{WT}::PV-cre (PVWT) mice, or App^{HOM}::SST-cre (SSTAPP) and App^{WT}::SOM-cre (SSTWT), respectively. $N = 3$ PVWT (2 male, 1 female), $N = 5$ PVAPP (5 male), $N = 2$ SSTWT (1 male, 1 female) and $N = 4$ SSTAPP (1 male, 3 female) mice were used for experiments. All procedures were carried out in accordance with the UK Animals (Scientific Procedures) Act 1986 and EU Directive 2010/63/EU and were reviewed by the University of Exeter Animal Welfare and Ethical Review Body.

2.2. Surgical implantation of electrodes

Surgical procedures were performed using aseptic techniques. APP and WT mice were anesthetised with isoflurane and placed in a stereotaxic frame (Stoelting, IL, USA). An incision was made in the scalp to expose the skull and microscrews (Antrin, CA, USA) were inserted into the frontal, parietal and interparietal plates bilaterally to anchor the implant to the skull. 1 mm diameter craniotomies were made over mPFC (in mm, from Bregma: AP = +1.75, ML = +0.25) and dorsal CA1 (in mm, from Bregma: AP = -2.0, ML = +1.4) and four-channel electrodes (Q1x4-5mm-200-177-CQ4, Neuronexus, MI, USA) were implanted to a depth (in mm, from the brain surface) of 1.7 (mPFC) and 1.5 (CA1), respectively. Silver wire (World Precision Instruments, FL, USA) and silver conductive paint (RS Components, Corby, UK) were used to connect the ground channel of each electrode array to an anchor screw overlying the cerebellum. Light-curable dental cement (RelyX Unicem, Henry Schein, NY, USA) was used to secure the electrodes to the skull and anchor screws, and the scalp was closed around the base of the implant using a suture. Subcutaneous carprofen (5 mg/kg) was used for the management of post-operative pain as required.

2.3. Electrophysiology data acquisition

Neural signals were acquired by connecting each electrode array to an Omnetics adapter (OM26, NeuroNexus) and headstage amplifier (RHD2000, Intan Technologies, CA, USA). The two headstages were connected to a dual headstage adapter (Intan) that allowed signals to be relayed along a single tether cable (Intan RHD SPI) to an OpenEphys acquisition board. Signals were bandpass filtered online at 0.1-7932 Hz and continuously recorded at 30 kHz. Signals recorded in CA1 in two mice (1 APP male; 1 WT female) were of poor quality (potentially due to poor grounding) and so were excluded from analysis.

Recordings commenced 8 weeks after surgery. Animals were recorded in their home cage for three hours during the lights-on circadian

epoch to enable recording of neural signals during sleep. An overhead light remained on throughout recording (440 lx). A Logitech colour webcam was fitted overhead (30 Hz frame rate) and videos were recorded throughout neural signal acquisition. To record neural activity during ambulation, animals were placed in a square open-field and allowed to explore for 1 h. Two light-emitting diodes (LEDs) were attached and grounded to one of the headstages that allowed the animal's position to be tracked using the software Bonsai (Lopes et al., 2015). Tracking data collected from Bonsai were acquired through the OpenEphys recording system at the same time as the neural signals. To allow for the LEDs to be visualised, all lights were switched off apart from an overhead LED light (1 lx).

2.4. Verification of electrode locations

At the end of experimental procedures, mice were deeply anaesthetised using an overdose of sodium pentobarbital (300 mg/kg) and electrolytic lesions were made at electrode sites. Mice were then transcardially perfused with 0.1 M phosphate buffer (PB) followed by 4% paraformaldehyde (PFA) in 0.1 M PB. Brains were extracted, postfixed in 4% PFA in 0.1 M PB overnight, and cryoprotected in 30% *w*/w sucrose in 0.01 M phosphate buffered saline (PBS). Brains were cut into 40 μm coronal sections using a freezing microtome (SM2010R, Leica Microsystems) and every fourth slice through mPFC and dorsal CA1 was mounted onto a slide and stained with DAPI. Sections were visualised using an epifluorescence microscope (Nikon Eclipse E800) and recording locations were confirmed from the lesions and electrode tracts. mPFC regions were defined based on previous literature (van de Werd et al., 2010), with electrode positions found in both the anterior cingulate cortex (ACC) and prelimbic (PL) cortex (***Supplementary Fig. 1A, B***). Hippocampal electrode placement was identified through histology and the changing polarity of SWRs in local field potential (LFP) traces recorded through the layers of CA1 (Buzsaki et al., 1992; Pelkey et al., 2015). Only electrodes located in *stratum pyramidale* (*Str.P*) were used for analysis (***Supplementary Fig. 1C, D***).

2.5. Viral injection surgery and two-photon imaging

PVWT, PVAPP, SSTWT and SSTAPP mice underwent similar surgical procedures as described above. The skull was exposed, and a craniotomy was made over dorsal CA1 (in mm, from Bregma: AP = -2.2, ML, +2.0). 250 nl of AAV9/2-CAG-dlox-GCaMP6f-dlox-WPRE-SV40 (5×10^{12} GC/ml) (Viral Vector Facility, University of Zurich) was infused into the CA1 region at a depth of 1.3 mm from the dura (rate: 50 nl/min) using a pulled glass micropipette and microinjection pump (World Precision Instruments). Three weeks after viral injection, mice were implanted with an optical cannula overlying dorsal CA1, as previously reported (Dombeck et al., 2010). Briefly, anaesthesia was induced using ketamine (73 mg/kg)/medetomidine (0.44 mg/kg) and maintained using isoflurane. The skull was exposed, and a 3 mm diameter craniotomy was drilled, centred on the previous injection site. The dura was removed, and a column of cortex was aspirated whilst continuously irrigating with chilled cortex buffer (in mM: NaCl 125, KCl 5, glucose 10, HEPES 10, $CaCl_2$ 2, $MgSO_4$ 2). A stainless-steel cannula (3 mm o.d.; 2.4 mm i.d.; 1.5 mm long) with a 3 mm diameter coverslip (Warner Instruments) affixed to one end (using NOA71 adhesive, Norland) was lowered into the craniotomy to the depth of the external capsule and was glued in position (Loctite). The skull was then sealed with dental cement (Simplex Rapid, Kemdent) and a metal head-fixation bar was affixed to the implant.

Recordings were performed under light (0.5-1%) isoflurane anaesthesia 150-240 min after initial induction of anaesthesia for surgery. Mice were transferred to a two-photon microscope and the head-fixation bar was secured using a clamp. Body temperature was maintained at 37 °C using a homeothermic blanket. A piezoelectric transducer beneath the thorax continuously monitored breathing rate as a proxy measure of anaesthetic depth, and the isoflurane dose was adjusted to maintain a consistent breathing rate between 150 and 200 breaths per minute. Images were acquired at 16× objective magnification (Nikon Plan Fluorite, 0.8 NA, 3 mm WD) using a microscope (Hyperscope, Scientifica) equipped with a Ti:sapphire pulsed laser (Chameleon Discovery, Coherent) and galvanometric scan mirrors. GCaMP6f was excited at 920 nm (power < 50 mW at the sample) and fluorescence was collected using a 500-550 nm emission filter. Images were acquired at 30 Hz using ScanImage 4.0 software (Pologruto et al., 2003). Spontaneous GCaMP6f signals were recorded continuously for 300 s. Signals were captured 200-300 μm beneath the external capsule in PVWT and PVAPP mice (around the depth of CA1 *Str.P*) and 100-200 μm beneath the external capsule in SSTWT and SSTAPP mice (around the depth of CA1 *Str. Oriens*). Several regions of interest (ROIs) (4.5 (3 7) [Med (Min Max)]) containing multiple GCaMP6f-positive neurons (5 (2 16) [Med (Min Max)]) were imaged per mouse.

2.6. Electrophysiology data analysis

All analysis was performed using custom-made scripts in MATLAB (Mathworks).

2.6.1. Detection of sleep states and sleep-associated neuronal oscillations

Periods of NREM and REM sleep were isolated from signals using an algorithm based on previously published work (Kohto et al., 2008; Witton et al., 2016). LFP signals were first split into 30 s epochs and a theta:SWO/delta (6-12 Hz:1-4 Hz) power ratio was created. If the power ratio in a 30 s epoch fell below a threshold (median + 1 SD), and was also accompanied by a lack of movement, the epoch was considered sleep. If an epoch did not meet this requirement, it was considered to be awake. These signals were put through the same algorithm using 10 s bins to further split sleep epochs into NREM and REM sleep (***Supplementary Fig. 2A***).

To analyse the dynamics of each of the three cardinal oscillations, custom-made detection scripts based on previously described methods were used to isolate and analyse individual oscillation cycles (Mölle et al., 2009; Nir et al., 2011; Phillips et al., 2012; David et al., 2013; Staresina et al., 2015; Latchoumane et al., 2017; Niethard et al., 2018; Bartsch et al., 2019). The SWO was detected by first low-pass-filtering the raw SWS signal (1.5 Hz) and all negative to positive zero-crossings were found. Two consecutive negative-positive zero-crossings within 0.25-2 s (0.5-1.25 Hz) of each other and the largest peak and trough between them were used in the next stage of detection. Events were classed as a SWO if the peak was greater than the 60th percentile of all detected peaks and the total amplitude (peak-trough) was also greater than the 60th percentile of all detected amplitudes.

For the detection of spindle (9-16 Hz) and ripple (130-250 Hz) events, the raw SWS signal was first bandpass filtered, z-scored and peaks were interpolated using cubic spline interpolation. Peaks that crossed a 3.5 SD threshold were identified and start and stop times of 1.5 SD either side were taken for the detection of spindles. A 6.5 SD threshold with 2 SD start and stop times were used for the detection of ripples. Events were then classed as spindles if they were between 0.5 and 2 s long and had an intra-spindle frequency of 11-15 Hz and as ripples if their duration was between 30 and 250 ms and had an intra-ripple frequency of 130-250 Hz.

For each oscillation, the duration, intra-oscillation frequency and incidence of oscillation events was obtained. Additionally, a short-time FFT was computed for individual spindle and ripple events. Spindle power was calculated as the total 11-15 Hz power using a 0.09 s time window (1/11 Hz) with 50% overlap. Ripple power was calculated as the total 130-250 Hz power using a 0.008 s time window (1/130 Hz) with 50% overlap.

2.6.2. Oscillation coupling

Analysis windows spanning 2 s on each side of detected Down states were used to analyse the phase-amplitude coupling (PAC) between

detected SWO events and gamma oscillations. Spindles were considered coupled to the SWO If the peak of a detected spindle event occurred within 1 s after the peak of a detected Down state. Sections of raw signal that began 2 s before the onset of the Down state and ended 2 s after the peak of the spindle event were used to analyse their PAC. Similar analysis methods were applied for the SWO and ripples, except a 0.5 s period after the ripple peak was used for PAC. If a ripple began within 2 s following the onset of a spindle, they were considered coupled.

2.6.3. Open field power analysis

The two LEDs attached to the headstage were used to track the animal's position. Time-points in which the LEDs failed to reach detection levels or occurred out of range of the OF were automatically rejected and adjoining data points linearly interpolated. Speed was initially computed in 1 s time-bins ranging from 1 to 30 cm/s using the position of the animal. The LFP was then split into corresponding 1 s time bins and the total power (area under the curve, trapezoid method) was found for theta (6-12 Hz), low gamma (30-60 Hz) and high gamma (60-120 Hz) oscillations. Spectral analysis was computed using the Chronux toolbox (Bokil et al., 2010), using the function *mtspecgramc*. 1 s time bins with 50% overlap were used as well as 3 tapers, with the resultant spectra normalised to total power. Gamma oscillations were defined based on identified peaks in the spectra and electrical noise at 50 Hz and 100 Hz (4th order IIR Butterworth Bandstop, 47-53 Hz and 97-103 Hz, respectively) was removed from the spectra for analysis.

2.6.4. REM sleep power analysis

Theta (6-12 Hz), low gamma (30-60 Hz) and high gamma (60-120 Hz) oscillation power was computed using the Chronux toolbox (Bokil et al., 2010), using the function *mtspecgramc*. 1 s time bins with 50% overlap were used as well as 3 tapers, with the resultant spectra log-transformed. An average of the values within each frequency band was taken.

2.7. Two-photon imaging analysis

Custom routines in MATLAB and FIJI software (Schindelin et al., 2012) were used. Mechanical drift was corrected by cross-correlation-based subpixel registration (Fienup et al., 2008) to the average of the first second (30 frames) of each image time series. Sum projection images were then used to manually draw ROIs around visually identified cell bodies, and cellular fluorescence time series, $F_{ROI}(t)$, were constructed by averaging the ROI pixels in each frame. A correction for neuropil contamination was applied, following $F_{ROI}(t) = F_{ROI\_}measured(t) - F_{ROI\_}neuropil(t) \times R$(Chen et al., 2013). The neuropil signal for each ROI ($F_{ROI\_}neuropil$) was calculated by averaging the pixels within a 2 μm annulus expanded around each ROI, excluding pixels within other cellular ROIs. R was the linear regression coefficient between the measured ROI signal and its neuropil signal. Slow drifts in the fluorescence time series were corrected by subtracting the 8th percentile in a 30 s window centred on each time point, and relative fluorescence time series ($\Delta F/F$) were calculated as $(F_{ROI}(t)-F0)/F0$, where F0 was the median of $F_{ROI}(t)$ after drift correction. To detect fluorescence transients, we calculated the SD of the 20-80th percentile of $\Delta F/F$, and identified contiguous samples that exceeded F0 + 2SD and had a peak amplitude of at least F0 + 7SD. For correlation analysis, we calculated, for each cell, the mean pairwise zero-lag cross correlation between the cell's $\Delta F/F$ trace and the $\Delta F/F$ traces of all other simultaneously recorded cells.

2.8. Immunohistochemistry

Animals were transcardially perfused and brains were removed and sectioned, as described above. Sections were first washed in PBS with 0.3% Triton X-100 (PBS-T) before being immersed in 100 mM glycine in PBS-T. Sections were then washed in PBS-T and incubated in blocking solution (3% goat serum in PBS-T) for 1 h. Primary antibodies (rabbit anti-PV, 1:5000, Swant or rabbit anti-$A\beta_{1\text{-}42}$, 1:1000, Cell Signalling Technology) were diluted in blocking solution, applied to the sections, and incubated overnight at 4 °C. The next day, sections were washed in PBS-T and incubated in blocking solution containing biotinylated goat anti-rabbit secondary antibody (1:250, Vector Laboratories) for 1 h at room temperature. Sections were then rinsed in PBS-T and incubated in blocking solution containing DyLight 488 Streptavidin (1:250, Vector Laboratories) for 1 h. Finally, sections were washed, mounted onto glass slides, and covered with glass cover slips with mounting medium containing DAPI.

Images for quantification were visualised at 10× magnification on a Scientifica SliceScope microscope with CoolLED pE-4000 light source and captured using a QImaging Retiga R1 camera. Representative images were acquired at 10× magnification on a Leica confocal laser scanning microscope. Only the right hemisphere was imaged and each brain region was sampled at a similar distance from bregma between animals. Brain regions were defined according to published criteria (van de Werd et al., 2010) and the Allen Brain Atlas (https://mouse.brainmap.org/). To quantify the number of PV-expressing interneurons, the cell counter plugin was employed using FIJI software (Schindelin et al., 2012). All cell counts were normalised to the brain region area. Three slices per brain region were quantified to obtain an average per mouse. Widespread $A\beta_{1\text{-}42}$ pathology was observed in both the mPFC and hippocampus in APP mice (***Supplementary Fig. 3***).

2.9. Statistical analysis

For two-photon imaging analysis, cell was used as the experimental unit (N) as amyloidopathy is a progressive pathology that affects different cells at different times, often dependent on proximity to Aβ aggregates (Busche et al., 2008). Nonetheless, cells within individual animals are not fully independent and may covary (Aarts et al., 2014). To control for the nesting of cell within animal, the data were modelled using generalised linear mixed effects models (GLMMs) that included 'animal' as a random factor, allowing by-animal random intercept and by-animal random slope (R, lme4 package). Event frequencies were expressed as the total number of events in 300 s and modelled in a GLMM with Poisson distribution and log link function. Event amplitudes were modelled in a GLMM with lognormal distribution to account for positive skew in the population distributions. Cellular correlations fit a normal distribution and were modelled in an LMM. The effect of genotype was assessed via likelihood ratio chi-squared test.

All other statistical testing was carried out using Prism 9 (GraphPad). Normality of the data was tested using a D'Agostino and Pearson test. A Mann-Whitney *U* test of comparable ranks was used for nonparametric data. All non-parametric results are displayed as box plots showing the median, range and the inter-quartile range (IQR). Power calculations were performed using G*Power 3 (Faul et al., 2007).

3. Results

As disruptions to the sleep cycle appear in both humans with AD and mouse models of amyloidopathy (Bubu et al., 2017; Sindi et al., 2018), it is important to first state that no statistically significant difference was found between genotypes in the time spent in awake states, NREM or REM sleep (***Supplementary Fig. 2B***).

3.1. The power of gamma oscillations is not altered across brain states

Gamma oscillations (30-120 Hz) group the firing of neurons into distinct epochs to enable precise encoding and retrieval of information (Colgin and Moser, 2010; Buzsaki and Wang, 2012). They can be found nested within theta oscillations during awake behaviour (Lisman and Jensen, 2013) and REM sleep (Rasch and Born, 2013) and within the cortical SWO during NREM sleep (Steriade et al., 1996; Valderrama

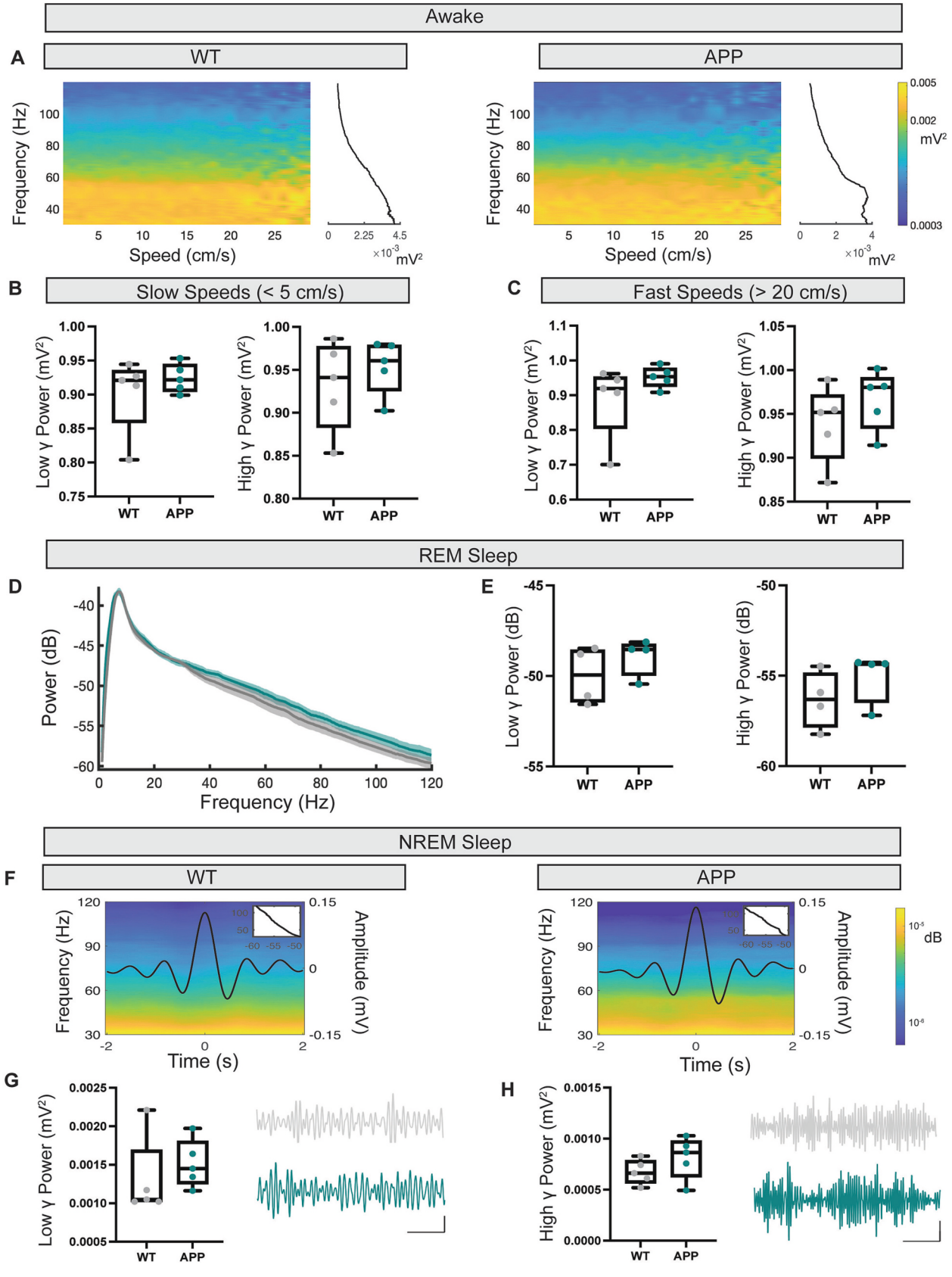

(caption on next page)

Fig. 1. No deficits to gamma oscillation power in mPFC. **A** Example spectrograms displaying a speed-modulated low and high gamma power in WT and APP mice. **B** No statistically significant difference was found to the power of low gamma (WT: 0.920 (0.859–0.936) vs APP: 0.922 (0.905–0.945) mV^2, U = 11, $p = 0.84$, Mann-Whitney *U* test) and high gamma (WT: 0.941 (0.883–0.977) vs APP: 0.961 (0.926–0.979) mV^2, U = 10, $p = 0.69$, Mann-Whitney U test) at slow ambulatory speeds. **C** No statistically significant difference was found to the power of low gamma (WT: 0.920 (0.804–0.953) vs APP: 0.954 (0.925–0.978) mV^2, U = 6, $p = 0.22$, Mann-Whitney *U* test) and high gamma (WT: 0.952 (0.899–0.972) vs APP: 0.980 (0.936–0.992) mV^2, U = 8, $p = 0.42$, Mann-Whitney *U* test) at fast ambulatory speeds. **D** Average power spectra ± SEM of both WT (grey) and APP (turquoise) CA1 LFPs during REM sleep. **E** No statistically significant difference was found to the power of low gamma (WT: -49.94 (-51.45 – -48.55) vs APP: -48.54 (-49.97 – -48.23) dB, U = 4, $p = 0.34$, Mann-Whitney U test) and high gamma (WT: -56.31 (-57.85 – -54.84) vs APP: -54.36 (-56.49 – -54.29) dB, U = 3, $p = 0.20$, Mann-Whitney *U* test) during REM sleep. **F** Example average SWO traces (black lines) overlaid on the corresponding LFP power spectrum showing the power of SWO-locked gamma oscillations for both WT and APP mice. Indented plots (top right corner) display the mean gamma power over the time-course of the LFP power spectrum. **G-H** No statistically significant difference was found to the power of low (WT: 0.0010 (0.0010–0.0017) vs APP: 0.0014 (0.0013–0.0018) mV^2, U = 6, p = 0.2, Mann-Whitney *U* test) and high gamma (WT: 0.00066 (0.00057–0.00079) vs APP: 0.00087 (0.00063–0.00098) mV^2, U = 6, $p = 0.22$, Mann-Whitney U test). Box plots show median, IQR and ranges. Descriptive statistics display median and IQR. (For interpretation of the references to colour in this figure legend, the reader is referred to the web version of this article.)

et al., 2012). Alterations to gamma oscillations have been identified during wakefulness in humans with AD (Murty et al., 2021) and in several mouse models of amyloidopathy (Verret et al., 2012; Castano-Prat et al., 2019; Jun et al., 2020; Gurevicius et al., 2013) along with the dysfunction of the inhibitory interneurons (Verret et al., 2012; Martinez-Losa et al., 2018; Hijazi et al., 2019) that drive them. We therefore hypothesised that similar impairments would be present in the mPFC and CA1 region of the hippocampus of APP mice during awake behaviour and in different sleep stages. However, in the mPFC no statistically significant change to the power of low (30-60 Hz) or high (60-120 Hz) gamma oscillations was identified in APP mice relative to WT when mice were ambulating at slow speeds (< 5 cm/s) or high speeds (> 20 cm/s) (Fig. 1A-C). There was also no difference between genotypes in low and high gamma oscillation power during REM sleep (Fig. 1B-E) and during SWO-nested gamma oscillations in NREM sleep (Fig. 1F-H).

Consistent with these results, no statistically significant change in gamma oscillation power was found in CA1 during awake behaviour at slow and fast ambulatory speeds (Fig. 2A-C) or in REM sleep when comparing APP with WT mice (Fig. 2D-E). Analysis of hippocampal SWO-nested gamma oscillations within NREM sleep was omitted from this analysis, as the function of these oscillations in this region are still to be elucidated. A potential reason for the lack of statistically significant power differences across brain states could be attributed to the larger variation within WT data compared with APP (Fig. 2B, C, E). It is therefore important to state that a *post-hoc* power calculation revealed that $N = 5$ mice per genotype is needed to reach the same statistical power as the statistically significant hippocampal data found in Fig. 3 (1-β: 0.69, α: 0.05). Yet, similar effect sizes can be found when comparing the statistically significant results in Fig. 3B (Cohen's *d*: 0.53) with the data in Figs. 2B (Cohen's *d*: 0.37 (low γ), 0.55 (high γ)), 2C (Cohen's *d*: 0.67 (low γ), 0.53 (high γ)) and 2E (Cohen's *d*: 0.51 (low γ), 0.52 (high γ)). Nevertheless, these results raised the question as to whether the dysfunction of other neuronal oscillations precedes gamma breakdown, which prompted us to focus our attention on the neuronal oscillations underlying memory consolidation in the hippocampal-mPFC circuit during NREM sleep.

3.2. Decreased ripple power and increased coordination of PV-expressing interneuron activity in the hippocampus in APP mice

Consolidation of newly acquired hippocampal memories occurs during NREM sleep as a result of the temporal communication between the cortical SWO, spindles and hippocampal SWR (Crunelli and Hughes, 2010; Maingret et al., 2016). SWR are oscillatory events that coincide with the replay of previously encoded information (Nádasdy et al., 1999) (Fig. 3A), with disruptions to these oscillations impairing the consolidation of hippocampus-dependent memories (Ognjanovski et al., 2017). As SWR are impaired in over-expression mouse models of amyloidopathy (Caccavano et al., 2020), we hypothesised that disruptions to SWR would also be seen in APP mice. A statistically significant decrease in the power of detected ripple events was found in APP mice (Fig. 3C), yet there was no change in the duration, frequency or occurrence of detected ripple events when compared with WT (Fig. 3 Bi, ii, iii).

Perisomatic-targeting PV+ interneurons play a key role in generating SWR (Ognjanovski et al., 2017; Stark et al., 2014; Gan et al., 2017), and their function is disrupted in several over-expression models of amyloidopathy (Verret et al., 2012; Martinez-Losa et al., 2018; Hijazi et al., 2019). We thus hypothesised that decreased ripple power in APP mice may be associated with altered PV+ cell function in CA1. Therefore, to measure PV+ cell activity, we generated APP and WT mice expressing Cre recombinase in PV+ neurons (PVAPP and PVWT mice, respectively) and imaged (Fig. 3E) Cre-dependent GCaMP6f in CA1 PV+ cells under consistent, light anaesthesia (***Supplementary Fig. 4***). Most cells (PVAPP = 95.5%; PVWT = 91.9%) exhibited spontaneous somatic Ca^{2+} events indicative of increased neuronal firing (Chen et al., 2013; Ali and Kwan, 2020), that often appeared coordinated between cells in the same field of view (Fig. 3F). There was no difference in event frequency or amplitude between PVAPP and PVWT interneurons (Fig. 3G, H). However, Ca^{2+} activity between simultaneously recorded PV+ cells was more correlated for PVAPP cells compared to PVWT (Fig. 3I). This suggests that Aβ pathology increased coordination of firing rate dynamics between PV+ interneurons without altering activity levels. Interestingly, this change to PV+ interneuron function was also accompanied by a statistically significant reduction in CA1 PV+ interneuron immunoreactivity in APP mice (Fig. 3D), suggesting that an increase in firing rate coordination may have manifested as a compensatory mechanism to combat reduced PV+ interneuron numbers. Since dysfunction in CA1 *oriens-lacunosum moleculare* (O-LM) interneurons has been reported in amyloid over-expression models (Schmid et al., 2016), we also measured spontaneous Ca^{2+} events from putative O-LM neurons in APP and WT mice expressing Cre recombinase in SST+ interneurons (SSTAPP and SSTWT mice, respectively). However, we observed no change in the frequency or amplitude of spontaneous Ca^{2+} events, or in the correlation of activity between SSTAPP and SSTWT cells (***Supplementary Fig. 5***). Thus, hypersynchronous firing of CA1 PV+ cells but not SST+ neurons (which include O-LM cells) may contribute to the observed reduction in ripple power.

3.3. Increased spindle power in the mPFC but no change to the SWO in APP mice

Given that SWRs were found to be impaired during NREM sleep, it was possible that the other neuronal oscillations responsible for long-term memory consolidation, the SWO and sleep spindles, were also affected. The SWO is the temporal pacemaker for systems consolidation and is composed of two distinct states, Up states and Down states (UDS), that reflect periods of synchronous depolarisation and firing followed by subsequent hyperpolarised epochs of relative quiescence (Steriade et al., 1993). Impairments to the SWO have been observed in both humans with AD (Mander et al., 2015b) and in mouse models of amyloidopathy (Castano-Prat et al., 2019; Busche et al., 2015; Kastanenka et al., 2017). However, when we analysed the UDS of the SWO in APP mice, no changes were found relative to WT (***Supplementary Fig. 6***).

The incidence of spindle (11-15 Hz) (Fig. 4A) oscillations during SWS

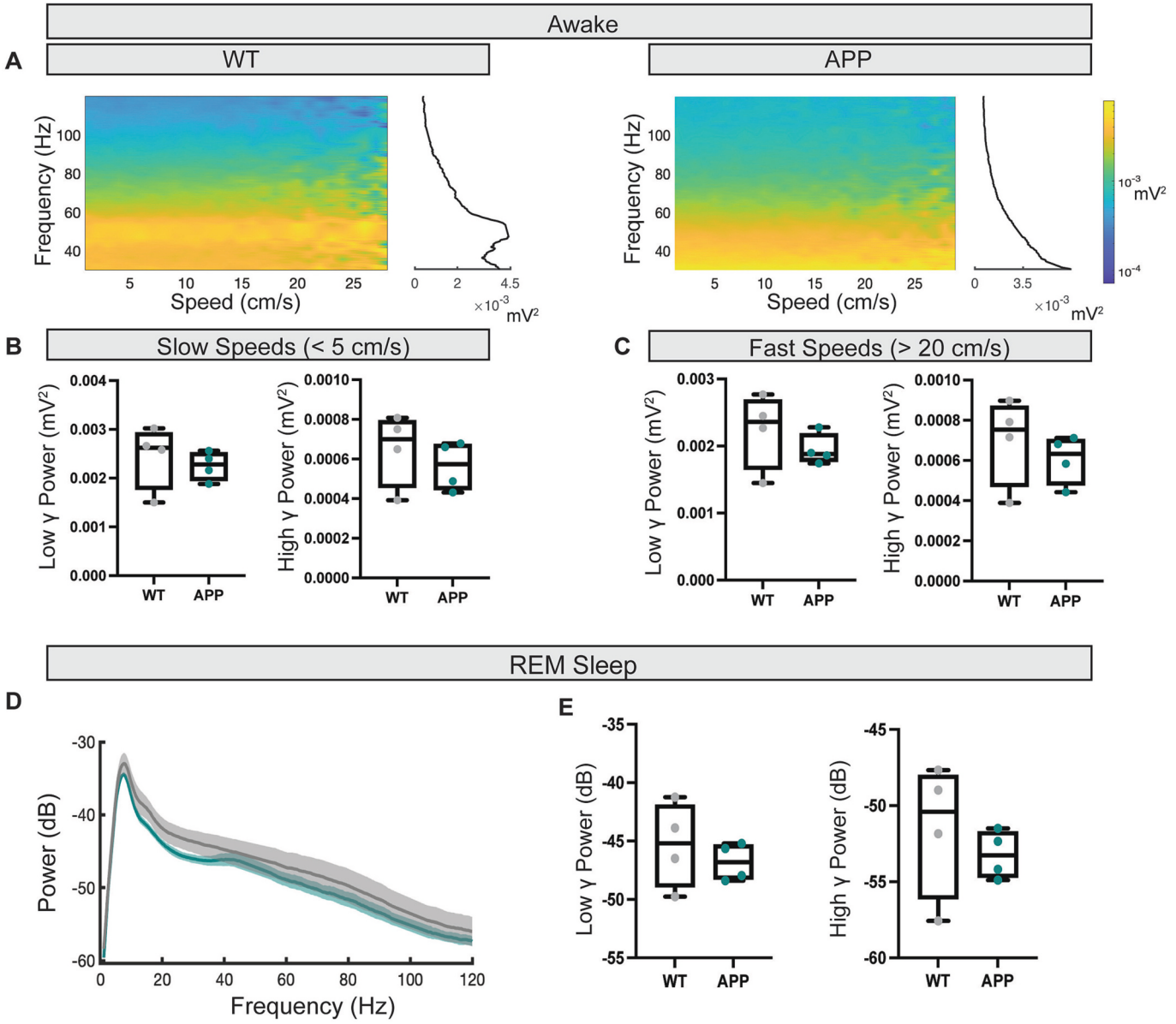

Fig. 2. No deficits to gamma oscillation power in CA1. **A** Example spectrograms displaying speed-modulated low and high gamma oscillation power in WT and APP mice. **B** No statistically significant difference was found to the power of low gamma (WT: 0.0020 (0.0017–0.0029) vs APP: 0.0023 (0.0020–0.0025) mV^2, U = 4, p = 0.34, Mann-Whitney U test) and high gamma (WT: 0.0006 (0.0004–0.0007) vs APP: 0.0006 (0.0004–0.0007) mV^2, U = 6, p = 0.68, Mann-Whitney U test) at slow ambulatory speeds. **C** No statistically significant difference was found to the power of low gamma (WT: 0.0024 (0.0017–0.0027) vs APP: 0.0018 (0.0017–0.0022) mV^2, U = 5, p = 0.49, Mann-Whitney U test) and high gamma (WT: 0.0007 (0.0005–0.0009) vs APP: 0.0006 (0.0005–0.0007) mV^2, U = 4, p = 0.34, Mann-Whitney U test) at fast ambulatory speeds. **D** Average power spectra ± SEM of both WT (grey) and APP (turquoise) CA1 LFPs during REM sleep. **E** No statistically significant difference was found to the power of low gamma (WT: -45.19 (-48.95 – -41.90) vs APP: -46.81 (-48.28 – -45.31) dB, U = 6, p = 0.67, Mann-Whitney U test) and high gamma (WT: -50.41 (-56.14 – -48.00) vs APP: -53.27 (-54.71 – -51.71) dB, U = 5, p = 0.49, Mann-Whitney U test) during REM sleep. Box plots show median, IQR and ranges. Descriptive statistics display median and IQR. (For interpretation of the references to colour in this figure legend, the reader is referred to the web version of this article.)

linearly correlates with subsequent memory performance in humans (Mölle et al., 2009), with a decrease in the number of detected spindles found in humans with AD (Kam et al., 2019). We found a statistically significant increase in the power of spindle events in the mPFC of APP animals relative to WT (Fig. 4C), with no change to their duration, frequency, or occurrence (Fig. 4 Bi, iii, iii). PV+ cells in the thalamic reticular nucleus (TRN) are involved in the generation of spindles (Clemente-Perez et al., 2017), while in the mPFC these interneurons are important in the feed-forward inhibition of incoming thalamocortical inputs (Delevich et al., 2015). Therefore, the density of these interneurons in the TRN and mPFC was assessed using immunohistochemistry. No change in PV+ cell density was found in the TRN (Fig. 4D) or in the ACC (Fig. 4E) or PL region of the mPFC (Fig. 4F). However, this does not negate functional impairments. Thus, it appears that SWR and spindles are altered in APP mice, whilst the SWOis spared.

3.4. Temporal communication between NREM sleep-associated neuronal oscillations is intact in APP mice

While the SWO, spindles and SWR play important functional roles in memory processing within the hippocampal-mPFC circuit, it is their temporal coupling that is thought to drive systems consolidation (Crunelli and Hughes, 2010; Maingret et al., 2016). Cortical spindles occur at the beginning of SWO Up states (Staresina et al., 2015; Mölle et al.,

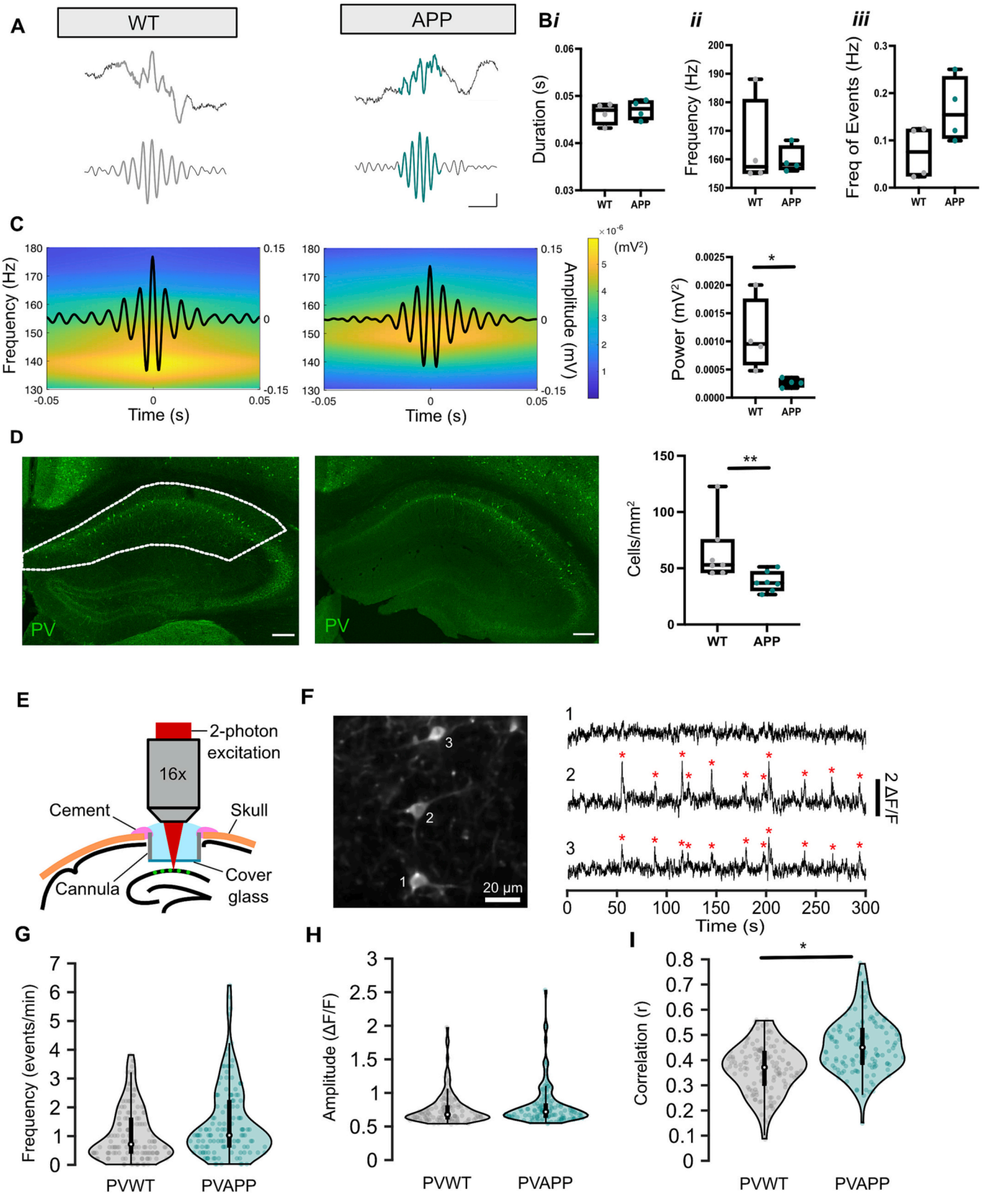

(caption on next page)

Fig. 3. Decreased power of hippocampal ripple events and increased coordination of PV-expressing interneuron activity in APP mice. **A** Example raw (top) and 130–250 Hz bandpass filtered (bottom) traces of detected ripple events from WT and APP mice (coloured segments). Scale bars: 20 ms, 50 μV (bottom), 100 μV (top). **B** No statistically significant difference was found in the average ripple duration (WT: 0.050 (0.044–0.048) vs APP: 0.047 (0.045–0.049) s, U = 5, $p = 0.48$, Mann-Whitney *U* test) ***(i)***, frequency (WT: 157.4 (155.2–180.9) vs APP: 158.3 (156.5–164.7) %, U = 7, $p = 0.88$, Mann-Whitney U test) ***(ii)*** or occurrence (WT: 0.08 (0.03–0.12) vs APP: 0.15 (0.10–0.23) Hz, U = 3, $p = 0.2$, Mann-Whitney U test) ***(iii)***. **C** Example average ripple traces (black lines) overlaid on corresponding LFP power spectra showing average ripple power. A statistically significant decrease in the average ripple power can be seen in APP mice compared with WT controls (WT: 0.00095 (0.00059–0.00175) vs APP: 0.00027 (0.00019–0.00034) mV^2, U = 0, $p = 0.02$, Mann-Whitney U test). **D** Representative images of PV+ interneurons within hippocampal CA1 of WT and APP mice. Scale bar: 200 μm. A statistically significant decrease in PV+ cell immunoreactivity was found in the CA1 hippocampal subregion of APP mice relative to WT (WT: 53.10 (46.22-75.59) vs APP: 36.92 (30.15-47.18) cells/mm^2, U = 4, $p = 0.007$, Mann-Whitney U test). **E** Schematic of two-photon imaging of PV+ neurons (green) in CA1 of the dorsal hippocampus. **F** Left: Two-photon image of three representative GCaMP6f-expressing cells in a PVWT mouse. Right: GCaMP6f fluorescence traces (ΔF/F) recorded from these cells. Red stars denote detected spontaneous Ca^{2+} events. **G-H** No statistically significant change was found in PVAPP cells ($N = 128$ cells, 28 (13 41) cells/mouse [Med (Min Max)]) compared with PVWT ($N = 134$ cells, 55 (20 59) cells/mouse [Med (Min Max)]) for event frequency (PVWT = 0.70 (1.21) vs PVAPP = 1.01 (1.62) events/min, $X^2(1,N = 262) = 0.08$, $p = 0.78$ **(G)** or amplitude (PVWT = 0.68 (0.19) vs PVAPP = 0.72 (0.19) ΔF/F, $X^2(1,N = 246) = 0.02$, $p = 0.90$) **(H)**. **I** A statistically significant increase in the zero-lag cross-correlation of Ca^{2+} activity between simultaneously recorded PV+ cells was found in PVAPP animals compared with PVWT (PVWT = 0.37 (0.13) vs PVAPP = 0.45 (0.14), $X^2(1,N = 262) = 5.10$, $p = 0.024$). Violin plots: marker, median; box, IQR; whiskers, lower-upper adjacent values. Box plots show median, IQR and ranges. Descriptive statistics display median and IQR unless otherwise stated. *$p < 0.05$, ** $p < 0.01$. (For interpretation of the references to colour in this figure legend, the reader is referred to the web version of this article.)

2002) while SWR soccur towards the end (Mölle et al., 2006). This coupling could be clearly seen in our recordings; the power of mPFC spindles and hippocampal SWR are locked to the SWO Up state that in intracerebral recordings appears as a negative deflection in the LFP (Nir et al., 2011; Timofeev and Bazhenov, 2005) (Fig. 5A, D). To assess the coupling strength between these oscillations, several different parameters were measured. No significant change was found in the phase-amplitude coupling (PAC) of the SWO with cortical spindles when comparing APP with WT mice (Fig. 5B). Additionally, there was no significant change in the time lag between the peak of the SWO Down states and the peak of cortical spindle events, nor was there a change in the percentage of SWO events that were coupled to a cortical spindle (Fig. 5C). Furthermore, no statistically significant change was found in APP animals relative to controls when looking at the PAC of the SWO with ripples (Fig. 5E), when comparing the time lag between the peak of the Down states with the peak of the ripple events (Fig. 5F), or when analysing the percentage of SWO events coupled to a ripple (Fig. 5F).

Next, we investigated the coupling of spindles with SWRs. Cortical spindles are initiated before hippocampal ripples (Siapas and Wilson, 1998; Clemens et al., 2007; Xia et al., 2017) (Fig. 6A); it is thought that spindles prime cortical neurons for plasticity-related changes by increasing dendritic Ca^{2+} (Niethard et al., 2018) just prior to information transfer from the hippocampus during a ripple (Wierzynski et al., 2009; Dong et al., 2016). A breakdown in this coupling could therefore have disastrous consequences for memory consolidation. Nonetheless, no statistically significant change was found in APP animals relative to WT controls in the time lag between the start of cortical spindles and hippocampal ripples (Fig. 6B), nor in the percentage of cortical spindles coupled to ripples (Fig. 6C). Finally, no significant difference was found in the occurrence of SWO events with both spindles and ripples when comparing APP animals with WT (Fig. 6D,E). Therefore, despite changes occurring to local spindle and SWR events in APP mice, the ability of the mPFC-hippocampal circuit to control the temporal precision of the neuronal oscillations mediating long-term consolidation remains intact.

4. Discussion

This report is the first to assess rhythmic network activity across different brain states in the $App^{NL\text{-}G\text{-}F/NL\text{-}G\text{-}F}$ mouse model. It is also the first study to comprehensively analyse hippocampal-mPFC circuit function during NREM sleep in a mouse model of amyloidopathy, although others have made enquiries along similar lines (Zhurakovskaya et al., 2019; Benthem et al., 2020). Across awake, REM and NREM brain states the power of gamma oscillations was unperturbed in both the mPFC and CA1 region of the hippocampus. However, during NREM sleep changes to cortical spindles as well as hippocampal ripples were observed in $App^{NL\text{-}G\text{-}F/NL\text{-}G\text{-}F}$ mice at sixteen months of age. These changes to NREM sleep-associated neuronal oscillations measured in local networks were not accompanied by deficits to the temporal coupling between different oscillations throughout the hippocampal-mPFC circuit. Finally, PV+ interneurons in CA1 were found to exhibit a higher degree of synchronous activity, and a decrease in PV+ interneuron density was identified in CA1. Taken together, these results indicate that, prior to the onset of spatial and contextual memory impairments, Aβ pathology changes PV+ interneuron-mediated inhibition in local neural circuits. This likely leads to disruption of local oscillatory dynamics specific to NREM sleep but without disrupting long-range communication between hippocampus and mPFC. These deficits may be a harbinger of subsequent breakdown of hippocampal and mPFC function in AD.

4.1. Gamma oscillations across brain states are unimpaired

During active exploration, gamma oscillations show altered power within the cortex and hippocampus of first-generation mouse models of amyloidopathy (i.e. mice overexpressing human APP with familial AD mutations) (Verret et al., 2012; Jun et al., 2020; Gurevicius et al., 2013; Jin et al., 2018). Therefore, it was hypothesised that similar disruptions to gamma oscillations would be found during active exploration in $App^{NL\text{-}G\text{-}F/NL\text{-}G\text{-}F}$ mice, as well as during REM and NREM sleep. However, no differences were identified in the power of either low or high frequency gamma oscillations in either wake, REM or NREM sleep, across both the mPFC and CA1 region of the hippocampus. This is in contrast to a previous study that discovered evidence for impaired CA1 high frequency gamma oscillations during spatial navigation in the $App^{NL\text{-}G\text{-}F/NL\text{-}G\text{-}F}$ model between seven-thirteen months of age (Jun et al., 2020). Possible explanations for this discrepancy could be our preferred use of wildtype littermate controls compared to non-littermate control mice used in the prior study (Jun et al., 2020), as well as our hippocampal data having low power. Nevertheless, first generation mouse models of amyloidopathy can display changes in gamma oscillations as early as 4 months of age (Verret et al., 2012; Gurevicius et al., 2013), with the current study performed in mice that are 16 months. It is therefore possible that when mutated App is expressed at more physiological levels, a more prolonged exposure to amyloid pathology is required for robust gamma oscillation impairments to manifest.

4.2. An increase in mPFC spindle power

An increase in the power of cortical spindles was identified in APP animals compared to WT controls. Additionally, no differences were found when analysing PV+ interneuron density in the TRN, ACC and PL cortex. However, given that PV+ interneuron function is documented to be impaired in first-generation mouse models of AD (Verret et al., 2012;

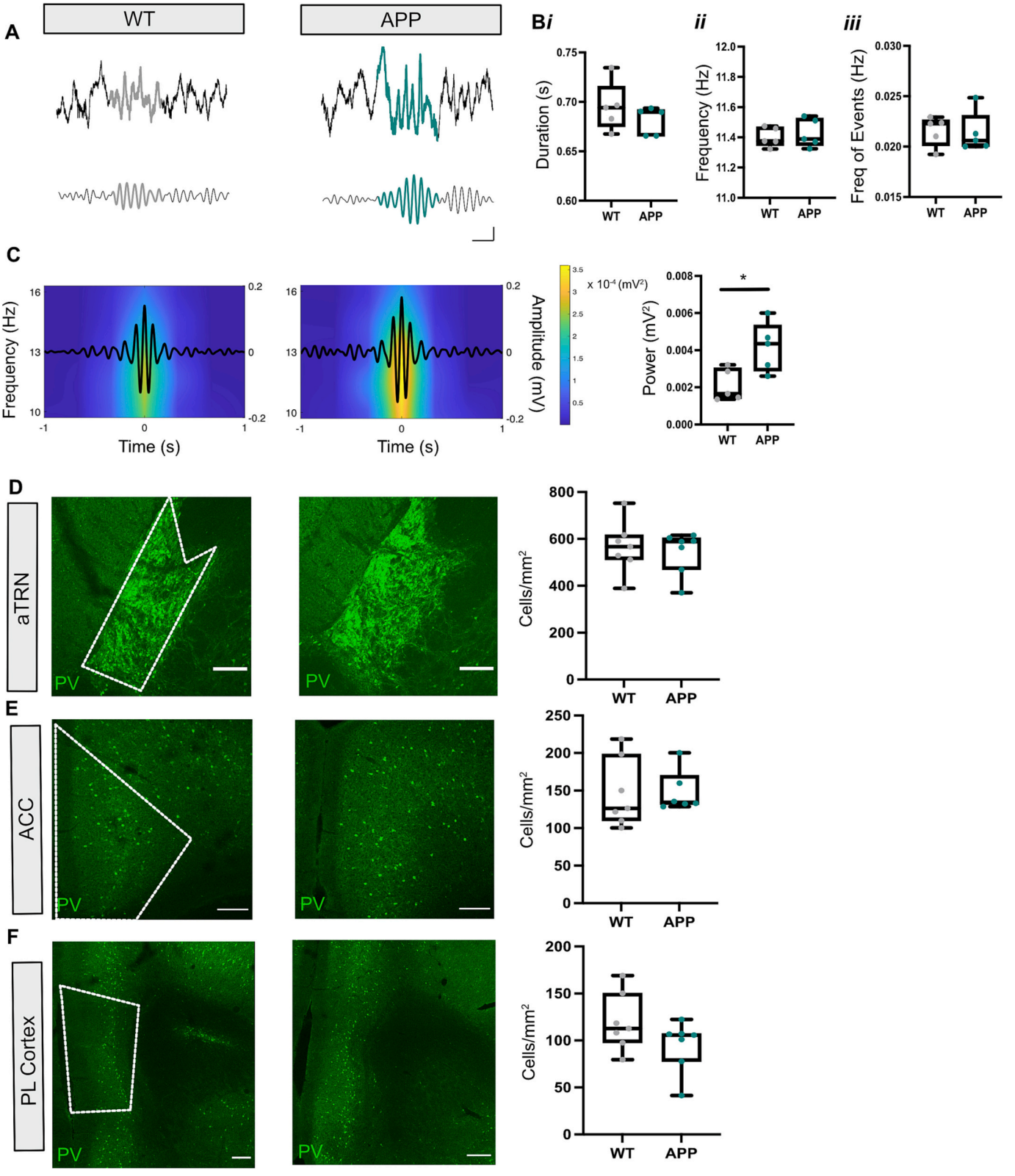

(caption on next page)

Fig. 4. Increased power of mPFC spindles in APP mice. **A** Example raw (top) and 11–15 Hz bandpass filtered (bottom) traces of detected spindle events (coloured segments) from WT and APP mice. Scale bars: 250 ms, 200 μV. **B** No statistically significant difference was found in APP animals relative to WT for the average spindle duration (WT: 0.69 (0.68–0.0.72) vs APP: 0.69 (0.67–0.69) s, U = 6, $p = 0.22$, Mann-Whitney *U* test) ***(i)*** and frequency (WT: 11.38 (11.35–11.47) vs APP: 11.39 (11.35–11.53) Hz, U = 10, $p = 0.69$, Mann-Whitney *U* test) ***(ii)***, nor was there a difference in the incidence of detected spindle events (WT: 0.022 (0.020-0.023) vs APP: 0.021 (0.020–0.023) Hz, U = 10, p = 0.69, Mann-Whitney U test) ***(iii)***. **C** Example average spindle traces (black lines) overlaid on the corresponding LFP power spectrum showing average spindle power. A statistically significant increase in the average spindle power was found in APP mice compared with WT controls (WT: 0.0017 (0.0014–0.0030) vs APP: 0.0043 (0.0029–0.0053) mV^2, U = 2.5, $p = 0.03$, Mann-Whitney U test). **D-F** Representative images of PV+ interneurons within the anterior thalamic reticular nucleus (aTRN) **(D)**, caudal anterior cingulate cortex (ACC) **(E)** and prelimbic (PL) cortex **(F)** of WT and APP mice. Scale bar: 200 μm. No statistically significant difference in PV+ cell immunoreactivity was found in the TRN between genotypes (WT: 567.1 (511.7-617.1) vs APP: 588.5 (469.0-604.5) Cell/mm^2, U = 23, $p = 0.90$, Mann-Whitney U test) or in the ACC (WT: 126.4 (110.0-198.5) vs APP: 134.2 (131.5-170.0) cells/mm^2, U = 15, $p = 0.44$, Mann-Whitney U test) or PL cortex (WT: 112.8 (97.51-150.2) vs APP: 105.7 (77.7-107.3) cells/mm^2, U = 13, $p = 0.16$, Mann-Whitney U test). Box plots show median, IQR and ranges. Descriptive statistics display median and IQR. $^*p < 0.05$.

Martinez-Losa et al., 2018; Hijazi et al., 2019) and that functional changes were identified to PV+ interneurons in the current study, this does not necessarily rule out impaired function. PV+ interneurons within the TRN help generate spindles (Latchoumane et al., 2017) by inhibiting the TC projection neurons of thalamic nuclei that in turn rebound-burst fire onto cortical neurons (Peyrache et al., 2011). Whereas in the mPFC, PV+ interneurons help gate this incoming excitatory input; preventing action potential propagation and localising increased Ca^{2+} to the dendrites to facilitate plasticity-related changes (Delevich et al., 2015). Therefore, any alterations to the activity patterns of PV+ interneurons have the potential to alter spindle dynamics and function. For example, a loss-of-function phenotype in mPFC PV+ interneurons can impair their gating capabilities and contribute to the increase in spindle amplitude. In turn, the failure of PV+ cells to regulate somatic and dendritic excitability could have disastrous ramifications for plasticity. However, this hypothesis is speculative and need to be investigated.

4.3. Disrupted hippocampal ripples and increased coordination of PV+ cell activity

Ripple events recorded in CA1 *Str.P* exhibited a statistically significant reduction in power, potentially suggesting disrupted spike-time dynamics between the PV+ interneurons and PCs that generate them. Indeed, CA1 PCs display impaired spiking during fast gamma oscillations in the $App^{NL\text{-}G\text{-}F/NL\text{-}G\text{-}F}$ mouse model (Jun et al., 2020), with both fast gamma oscillations and ripples requiring the recruitment of PV+ interneurons to modulate PC firing (Gan et al., 2017; Sohal et al., 2009). Moreover, PV+ interneuron spiking is reported to be impaired in first-generation mouse models of amyloidopathy (Verret et al., 2012; Martinez-Losa et al., 2018; Hijazi et al., 2019).

Ca^{2+} imaging revealed increased coordination of PV+ interneuron activity in CA1 in $App^{NL\text{-}G\text{-}F/NL\text{-}G\text{-}F}$ mice, yet these cells exhibited no change in their activity levels. A reduction in PV+ interneuron density accompanied these functional changes, implying that compensatory alterations may be occurring to the CA1 network as a result of PV+ interneuron loss. Compensatory remodelling of hippocampal inhibitory circuits as a result of aberrant neuronal activity has been previously described (Palop et al., 2007), with additional evidence suggesting that these alterations may ultimately become detrimental to the local circuitry (Hollnagel et al., 2019). Indeed, the increased coordination of PV+ cell activity could explain the observed decrease in ripple power. PV+ cells are involved in the pacing the ripple oscillation (Gan et al., 2017) and follow the spiking of PCs in the ripple trough (Stark et al., 2014). An increase in firing coordination could decrease the excitation-inhibition balance during each ripple cycle, resulting in a reduction in power and potential changes to PV+ interneuron – PC firing dynamics. This not only has the potential to disturb processes such as spike-time-dependant plasticity, but it could affect the recruitment of neurons for the reactivation of previously encoded information (Nádasdy et al., 1999), potentially interfering with consolidation. Future experiments recording the activity of both PCs and PV+ cells during SWRs in $App^{NL\text{-}G\text{-}F/NL\text{-}G\text{-}F}$ mice will give a clearer indication of how changes in PV+ interneuron activity contribute to dysfunctional oscillatory dynamics. Furthermore, given the reduced power of ripples, it would be interesting for future experiments to look at the spiking activity of neurons in the mPFC during a ripple event, to determine if the information contained within the ripple is being effectively transmitted to the cortex (Wierzynski et al., 2009; Dong et al., 2016).

4.4. The SWO and temporal communication within the hippocampal – mPFC circuit is spared

Although impairments were seen in both cortical spindles and hippocampal ripples, the temporal coupling between cardinal oscillations remained intact in sixteen-month-old APP mice. SWO coupling to cortical spindles was unaffected, suggesting that the TC feedback loop that controls their temporal communication is spared (David et al., 2013). Further evidence of spared communication between brain regions is our observation of intact coupling between the SWO and hippocampal ripples, cortical spindles with ripples, as well as the occurrence of all three cardinal oscillations together. This lack of coupling deficits is in line with no observable impairments to the SWO, which is considered the temporal pacemaker of the hippocampal – mPFC circuit during NREM sleep. Dysfunction of the SWO is reported in several over-expression mouse models of amyloidopathy (Castano-Prat et al., 2019; Busche et al., 2015; Kastanenka et al., 2017); therefore, like gamma oscillations, it is possible that amyloidopathy alone has no effect upon the SWO when mutated App is expressed at more physiological levels.

Taken together, these results suggest hippocampal-mPFC long-range communication is spared, with the changes occurring to the local oscillations constituting the first features of circuit dysfunction in $App^{NL\text{-}G\text{-}F/NL\text{-}G\text{-}F}$ mice. However, it is important to note that learning induces changes to oscillatory activity in the systems consolidation circuit: increased slow wave activity, spindle and ripple density, as well as an increase in spindle-ripple coupling are reported (Mölle et al., 2009). In some studies, Aβ-induced deficits to SWR dynamics were only identified during post-learning sleep following a hippocampus-dependant memory task, as opposed to during baseline conditions (Nicole et al., 2016; Jura et al., 2019). It is important to assess hippocampal-mPFC circuit function in baseline conditions without prior cognitive loading, however, as learning-induced changes could mask subtle neurophysiological deficits as biomarkers of AD. Yet, it is possible Aβ-induced deficits are more pronounced during active consolidation of hippocampus-dependant memories. Therefore, repeating experiments under these conditions may produce more striking deficits.

4.5. Relevance to the human condition

Gamma oscillations are considered a biomarker of network dysfunction in AD. Yet, studies conducted in humans produce varying results. Both increased and decrease gamma oscillation power have been identified, with no clear relationship between power, brain state or pathological state of the patients (Murty et al., 2021; van Deursen et al., 2008). These wide-ranging effects in humans coupled with the lack of

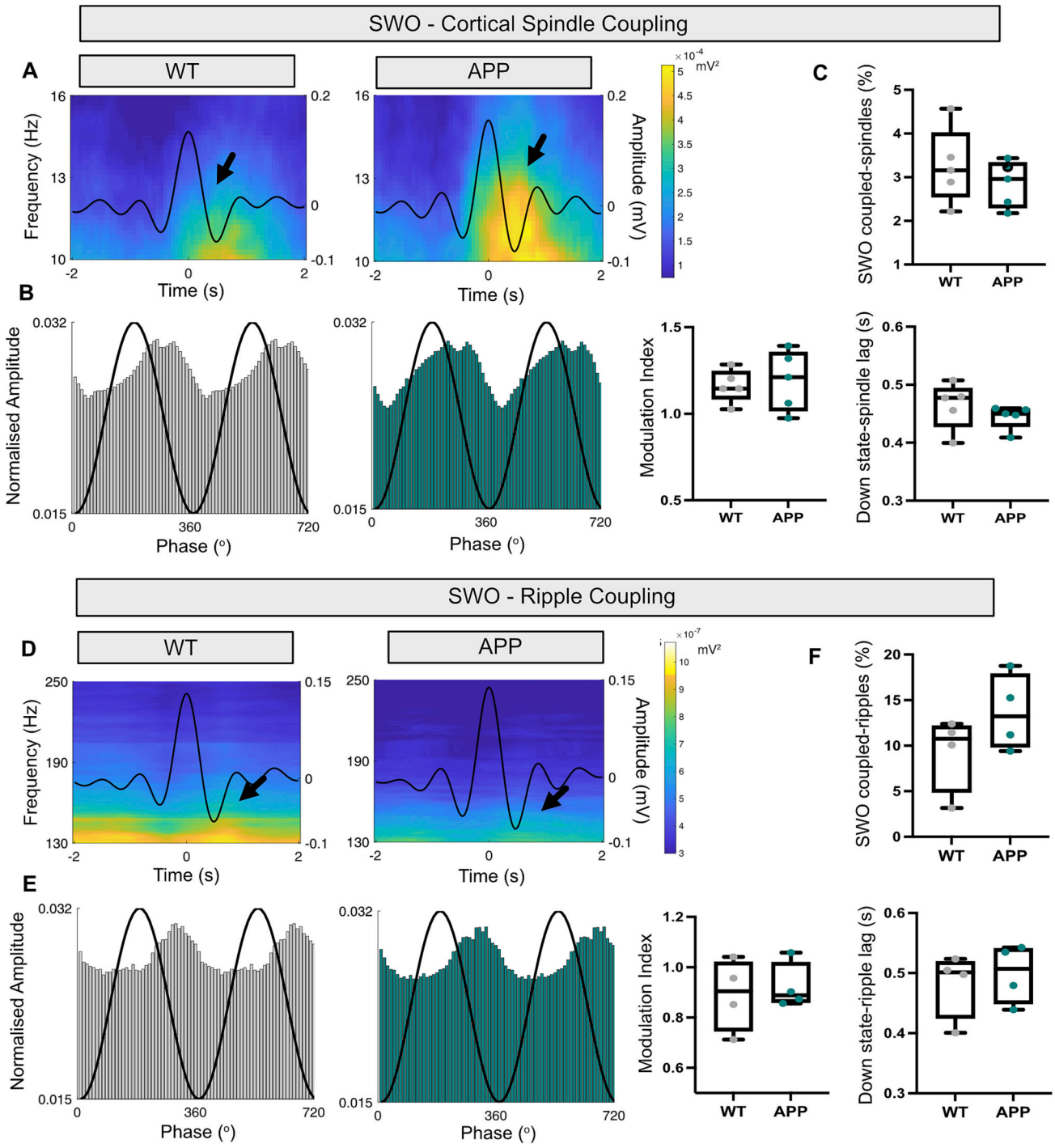

Fig. 5. Coupling of UDS with mPFC spindles and hippocampal SWR is not altered in APP mice during NREM sleep. **A** Example average UDS traces (black lines) overlaid on the corresponding LFP power spectrum showing the power of UDS-locked mPFC spindle oscillations for both WT and APP mice. Spindles can be seen locked to SWO Up states (black arrows). **B** No statistically significant difference in the PAC of UDS with mPFC spindle oscillations was found in APP animals relative to WT (WT: 1.15 (1.09–1.24) vs APP: 1.21 (1.02–1.36) MI, U = 10, $p = 0.65$, Mann-Whitney *U* test). Shown are example histograms of the change in normalised spindle amplitude (bars) over the phase of the UDS (black line) for both WT (left) and APP (right) mice. **C** No statistically significant difference was found in the time lag between the peak of the Down state to the peak of the mPFC spindle event (WT: 0.48 (0.43–0.49) vs APP: 0.45 (0.43–0.46) s, U = 7, $p = 0.31$, Mann-Whitney *U* test) or in the percentage of UDS coupled to a mPFC spindle event (WT: 3.16 (2.55–4.01) vs APP: 2.96 (2.30–3.33) %, U = 9, $p = 0.54$, Mann-Whitney U test). **D** Example average UDS traces (black lines) overlaid on the corresponding LFP power spectrum showing the power of UDS-locked ripple oscillations for both WT and APP mice. Ripples can be seen locked to SWO Up states (black arrows). **E** No statistically significant difference in the PAC of UDS with ripple oscillations was found between in APP animals compared with WT controls (WT: 0.90 (0.75–1.02) vs APP: 0.89 (0.86–1.02) MI, U = 6, $p = 0.68$, Mann-Whitney U test). Shown are example histograms of the changes to the normalised ripple amplitude (bars) over the phase of the UDS (black line) for both WT (left) and APP (right) mice. **F** No statistically significant difference was found in the time lag between the peak of the Down state to the peak of the ripple event (WT: 0.50 (0.42–0.52) vs APP: 0.51 (0.44–0.54) s, U = 6, p = 0.68, Mann-Whitney U test) or when looking at the percentage of UDS coupled to ripples (WT: 10.76 (4.89–12.15) vs APP: 13.23 (9.86–17.88) %, U = 5, $p = 0.48$, Mann-Whitney U test). Graphs show median and ranges. Box plots show median, IQR and ranges. Descriptive statistics display median and IQR.

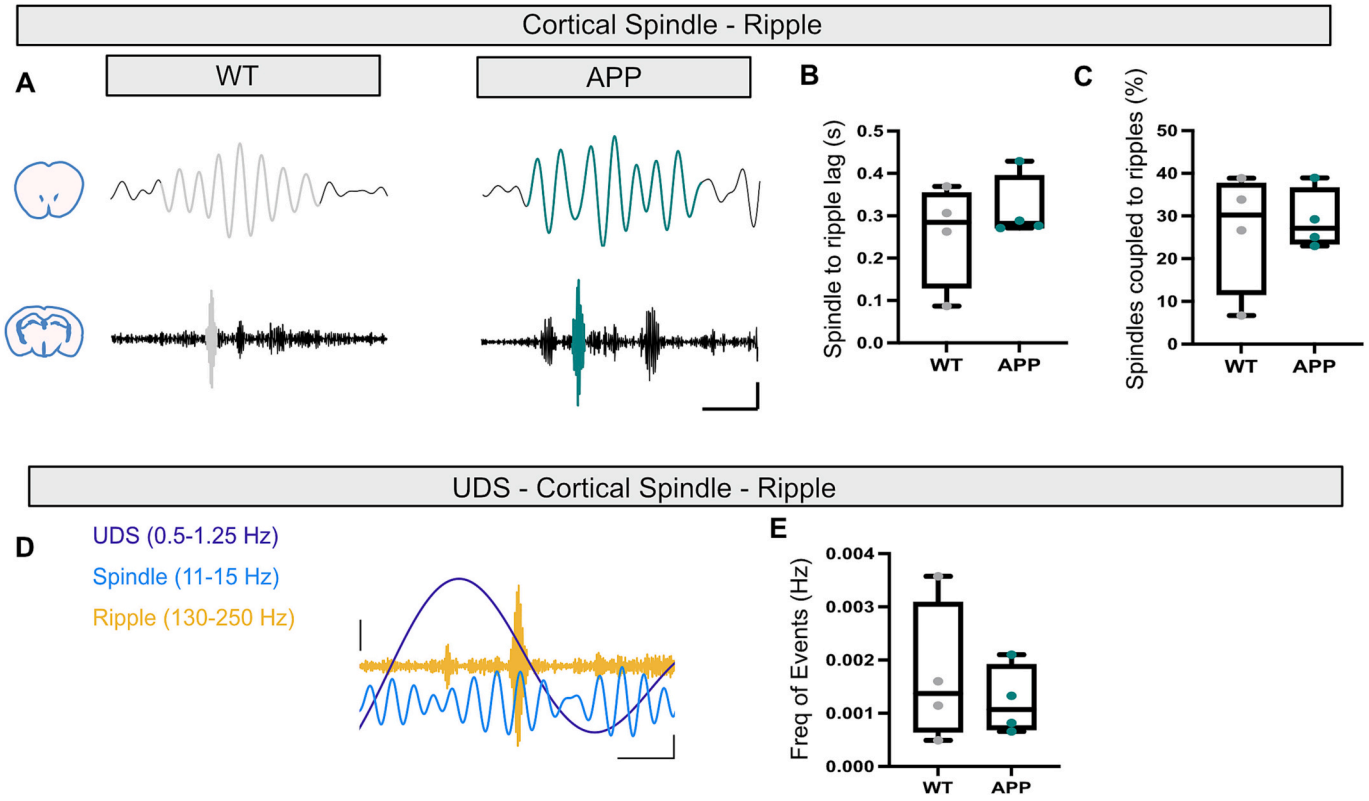

Fig. 6. UDS-spindle-ripple coupling is intact in APP mice. **A** Examples of 11-15 Hz bandpass filtered traces of spindle events in the mPFC (top) coupled to 130–250 Hz bandpass filtered CA1 ripple events (bottom) from WT and APP mice (coloured segments). Scale bars: 200 ms, 100 μV. **B** No statistically significant difference was found in the time lag between the start of mPFC spindle events to the start of CA1 ripple events (WT: 0.28 (0.13–0.35) vs APP: 0.28 (0.27–0.39) s, U = 6, $p = 0.68$, Mann-Whitney *U* test). **C** No statistically significant difference was found in the percentage of mPFC spindles coupled to CA1 ripples (WT: 30.24 (11.69–37.61) vs APP: 27.16 (23.51–36.52) %, U = 8, $p = 0.99$, Mann-Whitney U test). **D** Example of bandpass filtered traces showing the three cardinal oscillations occurring together in a WT mouse. UDS (0.5–1.25 Hz, purple), spindles (11–15 Hz, blue) and ripples (130–250 Hz, orange). Scale bars: 200 ms, 30 μV (right – UDS and spindle), 100 μV (left - ripple). **E** No statistically significant difference in the frequency of the three cardinal oscillations occurring together (WT: 0.00066 (0.00065–0.00308) vs APP: 0.0011 (0.00070–0.00190) %, U = 7, $p = 0.88$, Mann-Whitney U test). Box plots show median, IQR and ranges. Descriptive statistics display median and IQR. (For interpretation of the references to colour in this figure legend, the reader is referred to the web version of this article.)

statistically significant differences in gamma oscillation power in the present study suggest that impairments to these oscillations may not reflect an early or reliable instance of network dysfunction in AD. In fact, according to the data presented in this study, alterations to cortical spindle and hippocampal SWRs precede gamma oscillation breakdown and may potentially be a better marker of early network dysfunction as a result of amyloid pathology in AD.

The development of amyloid pathology is thought to precede and contribute to the cascade of pathophysiological impairments seen in AD (de Strooper and Karran, 2016). Additionally, sleep disruptions are common in the early stages of the disease and are thought to be a catalyst for further pathophysiological impairments (Holth et al., 2017). It is therefore possible that the App$^{NL\text{-}G\text{-}F/NL\text{-}G\text{-}F}$ mouse model of amyloidopathy reflects these early stages of AD progression, making it an ideal model for identifying biomarkers of early network dysfunction and investigating the initial causes of circuit breakdown. It is important that research into these early preclinical stages of AD is conducted, as it is likely that treatments targeting these stages are more effective (Aisen et al., 2022).

Author contributions

The project was conceived and designed by MTC, ESB and JW. All electrophysiological and immunohistochemical experiments and their analysis were conceived and conducted by ESB. Two-photon Ca^{2+} imaging experiments were conceived by JW and JG and conducted by JG with the help of JW, LA and MTC. TS and TCS provided the APP KI mouse line. Animal lines were bred and maintained by ESB, JG and LA. MTC and JW supervised and assisted the neurophysiological experimental work carried out by ESB and JG. EB, LA and MB carried out immunohistochemistry experiments and analysis. The manuscript was drafted by ESB and all authors discussed the results and critically revised the manuscript for intellectual content.

Funding

This work was supported by an Alzheimer's Research UK Interdisciplinary research grant ARUK-IRG2017B-4 (Michael T Craig), an Alzheimer's Research UK Fellowship ARUK-RF2015-6 (Jonathan Witton), an Alzheimer's Society Senior Fellowship AS-JF-14-007 (Francesco Tamagnini), and a Northcott Devon Medical Foundation grant TB/MG/NO5002 (Craig / Brady / Andrianova). Erica Brady was a GW4 BioMed doctoral training program student funded by the Medical Research Council (MR/N0137941/1), awarded to the Universities of Bath, Bristol, Cardiff and Exeter. Salary support for Lilya Andrianova was provided by Biotechnology and Biological Sciences Research Council grant BB/P001475/1 (Michael T Craig). The 2-photon imaging facilities were supported by Wellcome Trust multi-user equipment grant 202936/Z/16/Z (Andrew D Randall).

Declaration of Competing Interest

All authors report no competing interests.

Data availability

All raw data that supports the findings herein are available from the corresponding authors upon reasonable request.

Acknowledgements

The $APP^{NL-G-F/NL-G-F}$ mouse model was kindly supplied by MRC Harwell (UK).

Appendix A. Supplementary data

Supplementary data to this article can be found online at https://doi.org/10.1016/j.nbd.2023.106151.

References

Aarts, E., Verhage, M., Veenvliet, J., Dolan, C., van der Sluis, S., 2014. A solution to dependency: using multilevel analysis to accommodate nested data. Nat. Neurosci. 17, 491–496.
Aisen, P.S., Jimenez-Maggiora, G.A., Rafii, M.S., Walter, S., Raman, R., 2022. Early-stage Alzheimer disease: getting trial-ready. Nat. Rev. Neurol. 18 (7), 389–399.
Ali, F., Kwan, A.C., 2020. Interpreting in vivo calcium signals from neuronal cell bodies, axons, and dendrites: a review. Neurophotonics 7, 1.
Bakker, A., Krauss, G.L., Albert, M.S., Speck, C.L., Jones, L.R., Stark, C.E., et al., 2012. Reduction of hippocampal hyperactivity improves cognition in amnestic mild cognitive impairment. Neuron 74, 467–474.
Bartsch, U., Simpkin, A.J., Demanuele, C., Wamsley, E., Marston, H.M., Jones, M.W., 2019. Distributed slow-wave dynamics during sleep predict memory consolidation and its impairment in schizophrenia. NPJ Schizophr. 5, 1–11.
Benthem, S.D., Skelin, I., Moseley, S.C., Stimmell, A.C., Dixon, J.R., Melilli, A.S., et al., 2020. Impaired hippocampal-cortical interactions during sleep in a mouse model of Alzheimer's disease. Curr. Biol. 30, 2588–2601.e5.
Bokil, H., Andrews, P., Kulkarni, J.E., Mehta, S., Mitra, P.P., 2010. Chronux: a platform for analyzing neural signals. J. Neurosci. Methods 192, 146.
Born, H.A., 2015. Seizures in Alzheimer's disease. Neuroscience. 286, 251–263.
Bubu, O., Brannick, M., Mortimer, J., Umasabor-Bubu, O., Sebastião, Y., Wen, Y., et al., 2017. Sleep, cognitive impairment, and Alzheimer's disease: a systematic review and meta-analysis. Sleep. 40, 1–18.
Busche, M.A., Eichhoff, G., Adelsberger, H., Abramowski, D., Wiederhold, K.-H., Haass, C., et al., 2008. Clusters of hyperactive neurons near amyloid plaques in a mouse model of Alzheimer's disease. Science 321, 1686–1689.
Busche, M.A., Chen, X., Henning, H.A., Reichwald, J., Staufenbiel, M., Sakmann, B., et al., 2012. Critical role of soluble amyloid-β for early hippocampal hyperactivity in a mouse model of Alzheimer's disease. PNAS 109, 8740–8745.
Busche, M.A., Kekuš, M., Adelsberger, H., Noda, T., Förstl, H., Nelken, I., et al., 2015. Rescue of long-range circuit dysfunction in Alzheimer's disease models. Nat. Neurosci. 18, 1623–1630.
Buzsaki, G., Wang, X.-J., 2012. Mechanisms of gamma oscillations. Annu. Rev. Neurosci. 6, 2166–2171.
Buzsaki, G., Horvath, Z., Urioste, R., Hetke, J., Wise, K., 1992. High-frequency network oscillation in the hippocampus. Science 256, 1025–1027.
Caccavano, A., Bozzelli, P.L., Forcelli, P.A., Pak, D.T.S., Wu, J.-Y., Conant, K., et al., 2020. Inhibitory Parvalbumin basket cell activity is selectively reduced during hippocampal sharp wave ripples in a mouse model of familial Alzheimer's disease. J. Neurosci. 40, 5116–5136.
Castano-Prat, P., Perez-Mendez, L., Perez-Zabalza, M., Sanfeliu, C., Giménez-Llort, L., Sanchez-Vives, M.V., 2019. Altered slow (<1 Hz) and fast (beta and gamma) neocortical oscillations in the 3xTg-AD mouse model of Alzheimer's disease under anesthesia. Neurobiol. Aging 79, 142–151.
Chen, T.-W., Wardill, T.J., Sun, Y., Pulver, S.R., Renninger, S.L., Baohan, A., et al., 2013. Ultrasensitive fluorescent proteins for imaging neuronal activity. Nature 499, 295–300.
Chung, H., Park, K., Jang, H.J., Kohl, M.M., Kwag, J., 2020. Dissociation of somatostatin and parvalbumin interneurons circuit dysfunctions underlying hippocampal theta and gamma oscillations impaired by amyloid β oligomers in vivo. Brain Struct. Funct. 225, 935–954.
Clemens, Z., Molle, M., Eross, L., Barsi, P., Halasz, P., Born, J., 2007. Temporal coupling of parahippocampal ripples, sleep spindles and slow oscillations in humans. Brain 130, 2868–2878.
Clemente-Perez, A., Makinson, S.R., Higashikubo, B., Brovarney, S., Cho, F.S., Urry, A., et al., 2017. Distinct thalamic reticular cell types differentially modulate normal and pathological cortical rhythms. Cell Rep. 19, 2130–2142.
Colgin, L.L., Moser, E.I., 2010. Gamma oscillations in the hippocampus. Physiology 25, 319–329.
Crunelli, V., Hughes, S.W., 2010. The slow (<1 Hz) rhythm of non-REM sleep: a dialogue between three cardinal oscillators. Nat. Neurosci. 13, 9–17.
Dauwels, J., Srinivasan, K., Reddy, M.R., Musha, T., Vialatte, F.-B., Latchoumane, C., et al., 2011. Slowing and loss of complexity in Alzheimer's EEG: two sides of the same coin? Int. J. Alzheimers Dis. 2011, 1–10.
David, F., Schmiedt, J.T., Taylor, H.L., Orban, G., di Giovanni, G., Uebele, V.N., et al., 2013. Essential thalamic contribution to slow waves of natural sleep. J. Neurosci. 33, 19599–19610.
de Strooper, B., Karran, E., 2016. The cellular phase of Alzheimer's disease. Cell. 164, 603–615.
Delevich, K., Tucciarone, J., Huang, Z.J., Li, B., 2015. The mediodorsal thalamus drives feedforward inhibition in the anterior cingulate cortex via parvalbumin interneurons. J. Neurosci. 35, 5743–5753.
Dombeck, D.A., Harvey, C.D., Tian, L., Looger, L.L., Tank, D.W., 2010. Functional imaging of hippocampal place cells at cellular resolution during virtual navigation. Nat. Neurosci. 13 (11), 1433–1440.
Dong, X., Wang, V., Ikemoto, X.S., 2016. Coordinated interaction between hippocampal sharp-wave ripples and anterior cingulate unit activity. J. Neurosci. 36, 10663–10672.
Faul, F., Erdfelder, E., Lang, A.G., Buchner, A., 2007. G*Power 3: a flexible statistical power analysis program for the social, behavioral, and biomedical sciences. Behav. Res. Methods 39, 175–191.
Fienup, J.R., Guizar-Sicairos, M., Thurman, S.T., 2008. Efficient subpixel image registration algorithms. Opt. Lett. 33 (2), 156–158.
Gan, J., Ming, Weng S., Pernía-Andrade, A.J., Csicsvari, J., Jonas, P., 2017. Phase-locked inhibition, but not excitation, underlies hippocampal ripple oscillations in awake mice in vivo. Neuron 93, 308–314.
Gurevicius, K., Lipponen, A., Tanila, H., 2013. Increased cortical and thalamic excitability in freely moving APPswe/PS1dE9 mice modeling epileptic activity associated with Alzheimer's disease. Cereb. Cortex 23, 1148–1158.
Hijazi, S., Heistek, T.S., Scheltens, P., Neumann, U., Shimshek, D.R., Mansvelder, H.D., et al., 2019. Early restoration of parvalbumin interneuron activity prevents memory loss and network hyperexcitability in a mouse model of Alzheimer's disease. Mol. Psychiatry 25, 3380–3398.
Hollnagel, J.-O., Elzoheiry, S., Gorgas, K., Kins, S., Beretta, C.A., Kirsch, J., et al., 2019. Early alterations in hippocampal perisomatic GABAergic synapses and network oscillations in a mouse model of Alzheimer's disease amyloidosis. PLoS One 14, e0209228.
Holth, J.K., Patel, T.K., Holtzman, D.M., 2017. Sleep in Alzheimer's disease–beyond amyloid. Neurobiol Sleep Circadian Rhythms. 2, 4–14.
Hsieh, H., Boehm, J., Sato, C., Iwatsubo, T., Tomita, T., Sisodia, S., et al., 2006. AMPAR removal underlies Aβ-induced synaptic depression and dendritic spine loss. Neuron 52, 831–843.
Jin, N., Lipponen, A., Koivisto, H., Gurevicius, K., Tanila, H., 2018. Increased cortical beta power and spike-wave discharges in middle-aged APP/PS1 mice. Neurobiol. Aging 71, 127–141.
Jun, H., Bramian, A., Soma, S., Saito, T., Saido, T.C., Igarashi, K.M., 2020. Disrupted place cell remapping and impaired grid cells in a Knockin model of Alzheimer's disease. Neuron 107, 1–18.
Jura, B., Macrez, N., Meyrand, P., Bem, T., 2019. Deficit in hippocampal ripples does not preclude spatial memory formation in APP/PS1 mice. Sci. Rep. 9, 1–12.
Kam, K., Parekh, A., Sharma, R.A., Andrade, A., Lewin, M., Castillo, B., et al., 2019. Sleep oscillation-specific associations with Alzheimer's disease CSF biomarkers: novel roles for sleep spindles and tau. Mol. Neurodegener. 14, 1–12.
Kastanenka, K.V., Hou, S.S., Shakerdge, N., Logan, R., Feng, D., Wegmann, S., et al., 2017. Optogenetic restoration of disrupted slow oscillations halts amyloid deposition and restores calcium homeostasis in an animal model of Alzheimer's disease. PLoS One 12, 1–25.
Kohto, S., Taguchil, Y., Matsumoto, N., Wada, M., Huang, Z.-L., Urade, Y., 2008. Algorithm for sleep scoring in experimental animals based on fast Fourier transform power spectrum analysis of the electroencephalogram. Sleep Biol. Rhythms 6, 163–171.
Latchoumane, C.F., Ngo, H.V., Born, J., Shin, H.S., 2017. Thalamic spindles promote memory formation during sleep through triple phase-locking of cortical, thalamic, and hippocampal rhythms. Neuron 95, 424–435.
Lisman, J.E., Jensen, O., 2013. The theta-gamma neural code. Neuron. 77, 1002–1016.
Lopes, G., Bonacchi, N., Frazão, J., Neto, J.P., Atallah, B.V., Soares, S., et al., 2015. Bonsai: an event-based framework for processing and controlling data streams. Front. Neuroinform. 9, 7.
Maingret, N., Girardeau, G., Todorova, R., Goutierre, M., Zugaro, M., 2016. Hippocampo-cortical coupling mediates memory consolidation during sleep. Nat. Neurosci. 19, 959–964.
Mander, B.A., Marks, S.M., Vogel, J.W., Rao, V., Lu, B., Saletin, J.M., et al., 2015a. β-amyloid disrupts human NREM slow waves and related hippocampus-dependent memory consolidation. Nat. Neurosci. 18, 1051–1057.
Mander, B.A., Marks, S.M., Vogel, J.W., Rao, V., Lu, B., Saletin, J.M., et al., 2015b. β-amyloid disrupts human NREM slow waves and related hippocampus-dependent memory consolidation. Nat. Neurosci. 18, 1051–1057.
Martinez-Losa, M., Tracy, T.E., Ma, K., Verret, L., Clemente-Perez, A., Khan, A.S., et al., 2018. Nav1.1-overexpressing interneuron transplants restore brain rhythms and cognition in a mouse model of Alzheimer's disease. Neuron 98, 1–15.
Mölle, M., Marshall, L., Gais, S., Born, J., 2002. Grouping of spindle activity during slow oscillations in human non-rapid eye movement sleep. J. Neurosci. 22, 10941–10947.
Mölle, M., Yeshenko, O., Marshall, L., Sara, S.J., Born, J., 2006. Hippocampal sharp wave-ripples linked to slow oscillations in rat slow-wave sleep. J. Neurophysiol. 96, 62–70.
Mölle, M., Eschenko, O., Gais, S., Sara, S.J., Born, J., 2009. The influence of learning on sleep slow oscillations and associated spindles and ripples in humans and rats. Eur. J. Neurosci. 29, 1071–1081.

Murty, D.V.P.S., Manikandan, K., Kumar, W.S., Ramesh, R.G., Purokayastha, S., Nagendra, B., et al., 2021. Stimulus-induced gamma rhythms are weaker in human elderly with mild cognitive impairment and alzheimer's disease. Elife 10.
Nádasdy, Z., Hirase, H., Czurkó, A., Csicsvari, J., Buzsáki, G., 1999. Replay and time compression of recurring spike sequences in the hippocampus. J. Neurosci. 19, 9497–9507.
Nichols, E., Szoeke, C.E.I., Vollset, S.E., Abbasi, N., Abd-Allah, F., Abdela, J., et al., 2019. Global, regional, and national burden of Alzheimer's disease and other dementias, 1990–2016: a systematic analysis for the Global Burden of Disease Study 2016. Lancet Neurol. 18, 88.
Nicole, O., Hadzibegovic, S., Gajda, J., Bontempi, B., Bem, T., Meyrand, P., 2016. Soluble amyloid beta oligomers block the learning-induced increase in hippocampal sharp wave-ripple rate and impair spatial memory formation. Sci. Rep. 6, 22728.
Niethard, N., Ngo, H.-V., Ehrlich, I., Born, J., Hertie, D., 2018. Cortical circuit activity underlying sleep slow oscillations and spindles. PNAS 115, 9220–9229.
Nilsson, P., Saito, T., Saido, T.C., 2014. New mouse model of Alzheimer's. ACS Chem. Neurosci. 5, 499–502.
Nir, Y., Staba, R.J., Andrillon, T., Vyazovskiy, V.V., Cirelli, C., Fried, I., et al., 2011. Regional slow waves and spindles in human sleep. Neuron 70, 153–169.
Ognjanovski, N., Schaeffer, S., Wu, J., Mofakham, S., Maruyama, D., Zochowski, M., et al., 2017. Parvalbumin-expressing interneurons coordinate hippocampal network dynamics required for memory consolidation. Nat. Commun. 8.
Palop, J.J., Mucke, L., 2016. Network abnormalities and interneuron dysfunction in Alzheimer disease. Nat. Rev. Neurosci. 17, 777–792.
Palop, J., Chin, J., Roberson, E.D., Wang, J., Thwin, M.T., Bien-ly, N., et al., 2007. Aberrant excitatory neuronal activity and compensatory remodeling of inhibitory hippocampal circuits in mouse models of Alzheimer's disease. Neuron 55, 697–711.
Pelkey, K.A., Barksdale, E., Craig, M.T., Yuan, X., Sukumaran, M., Vargish, G.A., et al., 2015. Pentraxins coordinate excitatory synapse maturation and circuit integration of parvalbumin interneurons. Neuron 85, 1257–1272.
Peyrache, A., Battaglia, F.P., Destexhe, A., Sejnowski, T.J., 2011. Inhibition recruitment in prefrontal cortex during sleep spindles and gating of hippocampal inputs. PNAS 108.
Phillips, K.G., Bartsch, U., McCarthy, A.P., Edgar, D.M., Tricklebank, M.D., Wafford, K. A., et al., 2012. Decoupling of sleep-dependent cortical and hippocampal interactions in a neurodevelopmental model of schizophrenia. Neuron 76, 526.
Pologruto, T.A., Sabatini, B.L., Svoboda, K., 2003. ScanImage: flexible software for operating laser scanning microscopes. Biomed. Eng. Online 2, 1–9.
Rasch, B., Born, J., 2013. About sleep's role in memory. Physiol. Rev. 93, 681–766.
Saito, T., Matsuba, Y., Mihira, N., Takano, J., Nilsson, P., Itohara, S., et al., 2014. Single App knock-in mouse models of Alzheimer's disease. Nat. Neurosci. 17, 661–664.
Sasaguri, H., Nilsson, P., Hashimoto, S., Nagata, K., Saito, T., de Strooper, B., et al., 2017. APP mouse models for Alzheimer's disease preclinical studies. EMBO J. 36, 2473–2487.
Schindelin, J., Arganda-Carreras, I., Frise, E., Kaynig, V., Longair, M., Pietzsch, T., et al., 2012. Fiji: an open-source platform for biological-image analysis. Nat. Methods 9, 676–682.
Schmid, L.C., Mittag, M., Poll, S., Steffen, J., Wagner, J., Geis, H.-R., et al., 2016. Dysfunction of somatostatin-positive interneurons associated with memory deficits in an Alzheimer's disease model. Neuron 92, 114–125.
Shankar, G.M., Bloodgood, B.L., Townsend, M., Walsh, D.M., Selkoe, D.J., Sabatini, B.L., 2007. Natural oligomers of the Alzheimer amyloid-β protein induce reversible synapse loss by modulating an NMDA-type glutamate receptor-dependent signaling pathway. J. Neurosci. 27, 2866–2875.
Siapas, A.G., Wilson, M.A., 1998. Coordinated interactions between hippocampal ripples and cortical spindles during slow-wave sleep. Neuron 21, 1123–1128.
Sigurdsson, T., Duvarci, S., 2015. Hippocampal-prefrontal interactions in cognition, behavior and psychiatric disease. Front. Syst. Neurosci. 9, 190.
Sindi, S., Kåreholt, I., Johansson, L., Skoog, J., Sjöberg, L., Wang, H.X., et al., 2018. Sleep disturbances and dementia risk: a multicenter study. Alzheimer's Dementia 14, 1235–1242.
Sohal, V.S., Zhang, F., Yizhar, O., Deisseroth, K., 2009. Parvalbumin neurons and gamma rhythms enhance cortical circuit performance. Nature 459, 698–702.
Sperling, R.A., LaViolette, P.S., O'Keefe, K., O'Brien, J., Rentz, D.M., Pihlajamaki, M., et al., 2009. Amyloid deposition is associated with impaired default network function in older persons without dementia. Neuron 63, 178–188.
Staresina, B.P., Bergmann TO, Bonnefond, M., van der Meij, R., Jensen, O., Deuker, L., et al., 2015. Hierarchical nesting of slow oscillations, spindles and ripples in the human hippocampus during sleep. Nat. Neurosci. 18, 1679–1686.
Stark, E., Roux, L., Eichler, R., Senzai, Y., Royer, S., Buzsáki, G., 2014. Pyramidal cell-interneuron interactions underlie hippocampal ripple oscillations. Neuron 83, 467–480.
Steriade, M., Nunez, A., Amzica, F., 1993. A novel slow (<1Hz) oscillation of neocortical neurons in vivo: depolarizing and hyperpolariziong components. J. Neurosci. 73, 3252–3285.
Steriade, M., Contreras, D., Amzica, F., Timofeev, L., 1996. Synchronization of fast (30-40 Hz) spontaneous oscillations in lntrathalamic and thalamocortical networks. J. Neurosci. 76, 2788–2808.
Timofeev, I., Bazhenov, M., 2005. Mechanisms and biological role of thalamocortical oscillation. In: Columbus, F. (Ed.), Trends Chronobiol. Res. Nova Science Publishers, New York, pp. 1–47.
Valderrama, M., Crépon, B., Botella-Soler, V., Martinerie, J., Hasboun, D., Alvarado-Rojas, C., et al., 2012. Human gamma oscillations during slow wave sleep. PLoS One 7, e33477.
van de Werd, H.J.J.M., Rajkowska, G., Evers, P., Uylings, H.B.M., 2010. Cytoarchitectonic and chemoarchitectonic characterization of the prefrontal cortical areas in the mouse. Brain Struct. Funct. 214, 339–353.
van Deursen, J., Vuurman, E., Verhey, F., van Kranen-Mastenbroek, V., WJ R., 2008. Increased EEG gamma band activity in Alzheimer's disease and mild cognitive impairment. J. Neural Transm. 1301–1311.
Verret, L., Mann, E.O., Hang, G.B., Barth, A.M.I., Cobos, I., Ho, K., et al., 2012. Inhibitory interneuron deficit links altered network activity and cognitive dysfunction in Alzheimer model. Cell 149, 708–721.
Wierzynski, C.M., Lubenov, E., v., Gu M, Siapas AG., 2009. State-dependent spike-timing relationships between hippocampal and prefrontal circuits during sleep. Neuron 61, 587–596.
Witton, J., Staniaszek, L.E., Bartsch, U., Randall, A.D., Jones, M.W., Brown, J.T., 2016. Disrupted hippocampal sharp-wave ripple-associated spike dynamics in a transgenic mouse model of dementia. J. Physiol. 594, 4615–4630.
Xia, F., Richards, B.A., Tran, M.M., Josselyn, S.A., Takehara-Nishiuchi, K., Frankland, P. W., 2017. Parvalbumin-positive interneurons mediate neocortical-hippocampal interactions that are necessary for memory consolidation. Elife 6.
Zhurakovskaya, E., Ishchenko, I., Gureviciene, I., Aliev, R., Gröhn, O., Tanila, H., 2019. Impaired hippocampal-cortical coupling but preserved local synchrony during sleep in APP/PS1 mice modeling Alzheimer's disease. Sci. Rep. 9, 5380.